Chair of Physical Metallurgy

Master's Thesis

Microstructural influences on bending resonance fatigue in nickel-based superalloy Rene'88DT

Gregor Taurer, BSc

July 2024

MONTANUNIVERSITÄT LEOBEN
www.unileoben.ac.at

EIDESSTATTLICHE ERKLÄRUNG

Ich erkläre an Eides statt, dass ich diese Arbeit selbstständig verfasst, andere als die angegebenen Quellen und Hilfsmittel nicht benutzt, den Einsatz von generativen Methoden und Modellen der künstlichen Intelligenz vollständig und wahrheitsgetreu ausgewiesen habe, und mich auch sonst keiner unerlaubten Hilfsmittel bedient habe.

Ich erkläre, dass ich den Satzungsteil „Gute wissenschaftliche Praxis“ der Montanuniversität Leoben gelesen, verstanden und befolgt habe.

Weiters erkläre ich, dass die elektronische und gedruckte Version der eingereichten wissenschaftlichen Abschlussarbeit formal und inhaltlich identisch sind.

Datum 30.07.2024

Unterschrift Verfasser/in
Gregor Taurer

Acknowledgements

I am extremely grateful to my supervisors Dr. Ali Riza Durmaz, Fraunhofer Institute for Mechanics of Materials (IWM), and Dr. Oliver Renk, Chair of Physical Metallurgy at Montanuniversität Leoben. Their professional expertise and the discussions during the course of this thesis proved invaluable.

I would also like to thank the meso- and micromechanics group at the Fraunhofer Institute for Mechanics of Materials, especially Dr. Thomas Straub, Kilian Lombard, and Akhil Thomas, for their support with testing and coding-related issues.

Special thanks to Dr. Jean-Charles Stinville and his team at the University of Illinois Urbana-Champaign for analyzing micrographs with their Heaviside-DIC software and taking the time to answer my questions.

This thesis would not have been possible without my family and friends, to whom I am forever grateful.

Kurzfassung

Diese Masterarbeit behandelt die meso- und mikroskalige Ermüdung der Nickel-basierten Superlegierung Rene'88DT unter Verwendung von Biegeresonanzversuchen an flachen, mesoskaligen Proben, Rasterelektronenmikroskopie, und Datenanalyse. Die untersuchte Superlegierung wurde für die Hochdruck-Turbine von Jet-Triebwerken entwickelt, um eine noch längere Lebensdauer und Sicherheit zu erzielen, während auch die Effizienz und Nachhaltigkeit der Turbine verbessert werden.

Die vorgelegte Arbeit soll dabei helfen die Lücke zwischen experimentellen Daten aus Ermüdungsversuchen und Simulationen weiter zu schließen. Dabei wurden mikrostrukturelle Gegebenheiten identifiziert die häufig zum Auftreten eines Risses führen. Weiters wurde die lokale Mikrostruktur um die Rissentstehung mithilfe von high-resolution digital image correlation auf ihre sub-Korn-Dehnung untersucht.

Die Präparation, die Ermüdungsversuche und die Auswertung wurde mit state-of-the-art Methoden und Software durchgeführt und zielt dabei auf eine hohe Reproduzierbarkeit ab, eventuell auch für andere Werkstoffe.

Vorangegangene Untersuchungen wurden als Leitfaden betrachtet und bereits bestehende Theorien für mikrostrukturelle Einflüsse wurden auf ihre Validität getestet.

Die vorliegenden Ergebnisse bekräftigen die Abhängigkeit der Ermüdungsbeständigkeit und Schadenstoleranz (engl. Damage Tolerance, "DT") von mikrostrukturellen Charakteristika, wie Zwillingskorngrenzen und hohen Schmid-Faktoren. Die Rissentstehung an Zwillingskorngrenzen wurde genauer untersucht und wird in der vorliegenden Arbeit mit einem energiebasierten Modell für Gleitbandrisse, aufgrund des Wanderns von Versetzungen und einem damit verbundenen Aufstau an Korngrenzen, erklärt.

Abstract

This master's thesis delves into the meso- and microscale fatigue phenomena of nickel-based superalloy Rene'88DT by utilization of bending resonance fatigue testing of flat mesoscale specimens, scanning electron microscopy, and data analysis. The alloy was developed for the high-pressure turbine section of large gas turbine engines in pursuance of higher lifetime and safety, while simultaneously increasing the efficiency and sustainability of the engine.

This work aspires to reduce the hiatus between experimental results of fatigue damage in high-pressure turbine disks and the computational simulation and design process by identifying microstructural influences on fatigue crack initiation. Moreover, using high-resolution digital image correlation allows to measure the sub-grain strain that developed near fatigue crack initiation sites.

The preparation, testing, and evaluation were done with state-of-the-art methods and software, aiming for high reproducibility and possible application to other complex materials. Preceding studies served as a guide and some of the existing theories for microstructural influences were tested for their validity.

The results are consistent with the literature of fatigue damage occurring during fully reversed axial fatigue testing. Fatigue crack initiation was predominantly discovered near twin boundaries and a suitable model for energy-based slip band cracking due to dislocation motion and pile-up was examined with the generated results from this thesis.

Table of contents

List of figures

List of tables

Nomenclature

Acronyms / Abbreviations

BCC	Body-centered cubic
(HD)BSD	(High-definition) backscattered electron detection
CI	Confidence index
3D CP-XFEM	3D crystal plasticity extended finite element modeling
CSL	Coincidence site lattice
DCT	X-ray diffraction contrast tomography
(HR)DIC	(High-resolution) digital image correlation
DT	Damage tolerant
EBSD	Electron backscatter diffraction
FCC	Face-centered cubic
FCGR	Fatigue crack growth rate
FE	Finite element
FIB	Focused ion beam
f_{res}	Resonance frequency
GB	Grain boundary
GC	Grain cluster
GE	General Electric

HAGB	High-angle grain boundary
HCF	High-cycle fatigue
HDIC	Heaviside digital image correlation
IPF	Inverse pole figure
IQ	Image quality
LAGB	Low-angle grain boundary
LCF	Low-cycle fatigue
LLF	Long-life fatigue
LUT	Look-up table
OPS	Oxide particle suspension
PIL	Python image library
PM	Powder metallurgy
PSB	Persistent slip band
ROI	Region of interest
RT	Room temperature
SEM	Scanning electron microscope
SFE	Stacking fault energy
SF	Schmid factor
TB	Twin boundary
TEM	Transmission electron microscope
T_m	Melting point
UTS	Ultimate tensile strength
V_f	Volume fraction
VHCF	Very-high-cycle fatigue

Chapter 1

Introduction

Nickel-based superalloys unite the necessary properties to withstand extreme environments such as the operation in a high-temperature, high-speed, and highly oxidizing setting—the gas turbine engine of an aircraft. Their evolution goes hand-in-hand with the improvements in sustainability and efficiency of air travel by being more powerful and less fuel-consumptive than in the past [1].
In order to reach this goal, a thorough understanding of the mechanisms that cause the material to fatigue is necessary to further improve these highly-stressed alloys. Fatigue damage is accumulated over thousands of hours of service and correct estimations must be made about critical crack sizes and their initiation. Only then can higher-output turbines ensure a safe and reliable operation. The relevant material for this thesis is Rene'88 Damage Tolerant (DT) which was introduced into service by General Electric (GE) in the early 1990s and is an improved version of Rene'95 [2]. This nickel-based superalloy is commonly used in aircraft and power-generating gas turbines in the disks of the turbine section, where it connects the shaft and the blades. The rotation speeds can reach up to 20,000 revolutions per minute, while temperatures reach up to 650 °C [1]. In this regard, a balance between creep strength, tensile strength, and damage tolerance is essential for a reliable and durable operation of the turbine [2]. Damage tolerance (see also section 2.2) refers to a concept where initial flaws (e.g., pores, inclusions) or sustained flaws (e.g., scratches, dents) do not lead to complete failure immediately, but the part's integrity remains at least until the next inspection [3].

Single crystal materials or ceramic matrix composites—known for their superior creep strength due to the elimination of grain boundaries—are used for the turbine blades. They are attached to the disk with special stress-reducing joints, such as the fir-tree joint. Current designs also include the "blisk", a disk with integrated blades, removing joints entirely [4].

In this master's thesis, the author tried to analyze comparable studies and former investigations and to compare them to the results in bending resonance fatigue, thereby furthering

the understanding of crack initiation and propagation in nickel-based superalloy Rene'88DT and assisting with prospective developments, both in designing and testing of superalloys.

In chapters three and four, the preparation and testing of the Rene'88DT mesoscale bending resonance fatigue specimens are described. These steps were necessary to reduce the thickness of the samples to the desired values, reduce stress concentrations at edges, provide a clean and deformation-free surface of the samples for proper electron microscopy, and ultimately to test the samples at their resonance frequency to initiate cracks at the surface, where the maximum stress is present. Part of the thesis was also the validation of the bending resonance fatigue setup for testing of nickel-based superalloys, operating in a fully reversed bending mode. The fifth chapter describes the computational analysis of the generated data from the first two sections. This includes the evaluation of the EBSD scans that were performed before fatigue testing and the assessment of the backscattered electron images that were taken before and after testing. Only the combination of the EBSD and HDBSD images allowed to relate crack initiation and propagation to the microstructure. The backscattered electron images ensured superior resolution of microcracks and also gave an indication of the microstructure due to the orientation contrast, making it easy to find the microcrack sites in the EBSD maps. The crystallographic information from the EBSD scans made it possible to evaluate ROIs for local differences in Schmid factor and grain boundary angle. Darkfield images were a valuable tool to monitor the surface in real-time during the bending resonance fatigue test and to utilize these images to trace back the location and cycle number for crack initiation.

Moreover, a routine for doing ex-situ high-resolution digital image correlation (HRDIC) in connection with EBSD was established based on an open-source code within Python.

Chapter 2

Literature

2.1 The nickel-based superalloy Rene'88DT

Rene'88DT was developed by GE Aerospace following the ENSIP[1] requirements of the United States Air Force in 1983 and was introduced at the 1992 Superalloys conference of *The Minerals, Metals & Materials Society* following a four-year research program [2]. Newly introduced in the ENSIP was the criterion for damage tolerance—the component's resistance to fatigue crack growth. Such cracks may start at initial flaws in the material such as defects or inclusions, introduced during the manufacturing process, or generally as a consequence of cyclic loading, i.e., fatigue-induced damage [3]. The initiation and propagation of these cracks, especially with respect to the microstructural properties, is the subject of research in this thesis. The aims for the development of Rene'88DT were "a 50 % reduction of the cyclic fatigue crack growth rate (FCGR, from RT-1200 °F); 25 °F minimum improvement in creep and stress-rupture strength; 10 percent maximum reduction in tensile strength"[2] compared to the nickel-based superalloy Rene'95 [2]. This was empirically tested in various setups for 23 experimental compositions through altering the chemical composition of the base alloy Rene'95. Alloy W2, later given the name Rene'88DT, emerged as the best option with contents of alloying elements as seen in table 2.1.

---

1 ENgine Structural Integrity Program

2 1200 °F converts to roughly 650 °C and Δ25 °F is understood as roughly 14 °C. The temperature increase in creep strength is understood as a measure of how much the temperature can be increased to achieve the same or lower creep strain.

Table 2.1 Chemical composition of Rene'95 and Rene'88DT (weight percent).

Alloy	Co	Cr	Mo	W	Al	Ti	Nb	B	C	Zr	Ni
Rene'95	8	13	3.5	3.5	3.5	2.5	3.5	0.015	0.03	0.03	bal
Rene'88DT	8	16	4	4	2.1	3.7	0.7	0.015	0.03	0.03	bal

2.1.1 Microstructure and the role of γ'

A highly alloyed material such as Rene'88DT would display large dendritic segregations and high thermal stresses in a conventional melting and casting process, therefore a route known as powder metallurgy (PM) is utilized [5]. The PM process for a turbine disk can be described following Prasad and Gessinger [5, 6]; first the raw materials and other constituents are molten in vacuum induction melting and subsequently turned into a fine powder by inert-gas atomization. The powder is then compacted by hot isostatic pressing, sometimes combined with a forging process. In order to achieve a fine and homogeneous distribution of gamma prime precipitates, the superalloy is then heat treated for one hour at 1150 °C to reach a super-solvus solution, following a delayed oil quench and an aging treatment for eight hours at 760 °C. Two gamma prime (γ') variants are formed during this heat treatment; a coarser secondary γ' during the cooling from super-solvus solution and a fine tertiary gamma prime during aging [7].

This gamma prime is a coherent, ordered precipitate with $L1_2$ structure and a constitution of Ni_3Al. A model of the crystal structure is shown in fig. 2.1a. It is the main strengthening phase in the face-centered cubic (FCC) solid solution nickel matrix. The γ' crystal planes are coherently ordered within the surrounding γ matrix. The yield-stress anomaly—an increase of yield strength with increasing temperature, due to the Kear-Wilsdorf mechanism—is also attributed to the γ' phase [8, 9]. The lattice distortion, due to the differences in lattice constants, is defined by the mismatch parameter δ:

$$\delta = 2 * \frac{a_p - a_m}{a_p + a_m} \tag{2.1}$$

a_p...lattice parameter precipitate (0.35917 nm for secondary γ', 0.35923 nm for tertiary γ')
a_m...lattice parameter matrix (0.3590 nm) [10]

The mismatch is about 0.05 % for Rene'88DT, allowing the precipitates to form homogeneously throughout the matrix. This low δ can be attributed to the considerate use of tungsten, which increases the lattice parameter of a_m without having an effect on a_p. The shape of the secondary γ' precipitates is dependent on the cooling rate after super-solvus solution:

spherical for high cooling rates, cuboidal/spheroidal for cooling rates around 100 °C/min, and dendritic for lower cooling rates. The shape of the tertiary γ' is independent of the cooling rate and is always spherical. No primary γ' is existent in the microstructure, due to the super-solvus heat treatment [7]. Prasad, however, claims that for nickel-based superalloys in general, the shape of secondary γ' is dependent on its volume fraction (V_f) and will change from spherical to more cuboidal for higher fractions, owing to the minimization of interfacial energy. This is also mentioned in Ref. [2], where the intragranular γ' size appears to be a function of V_f.

Concerning the size of the precipitates, secondary γ' is about 100-200 nm, as is evident from fig. 2.1b. Tertiary γ' ought to be around 1 nm in diameter and is therefore not visible in scanning electron microscope (SEM) images. Only with the right sample preparation and a transmission electron microscope (TEM) such fine particles can be resolved [7]. The size and volume fraction of the precipitates were subject of many investigations, as they play a prominent role in the evolution of fatigue damage in Rene'88DT. Krueger et al. [2] described that a reduction in γ' size would facilitate dislocation cutting and thus lead to planar slip (heterogeneous deformation), while larger precipitates would necessitate looping of the dislocations (i.e. Orowan strengthening) and therefore wavy slip. Moreover, they then claimed that fatigue crack growth rates decrease for smaller γ' precipitate sizes, because planar slip favors fully reversible dislocation motion and therefore reduces the plastic strain around that area. Furthermore, it was described that an increase in grain size had a positive effect on fatigue damage, while it simultaneously increases the creep strength of polycrystalline materials. This is because smaller grains have a higher ratio of grain boundary (GB) length by grain area in 2D sections or grain boundary area by grain volume in 3D sections. Hence, GB diffusion is promoted for finer grain sizes, resulting in Coble creep [2, 7]. The total γ' volume fraction in Rene'88DT is around 40 %. This relatively low γ' content of precipitates was found to have a positive impact on the FCGR at temperatures around 400 °C and a greater resistance to cracks occurring during quenching.

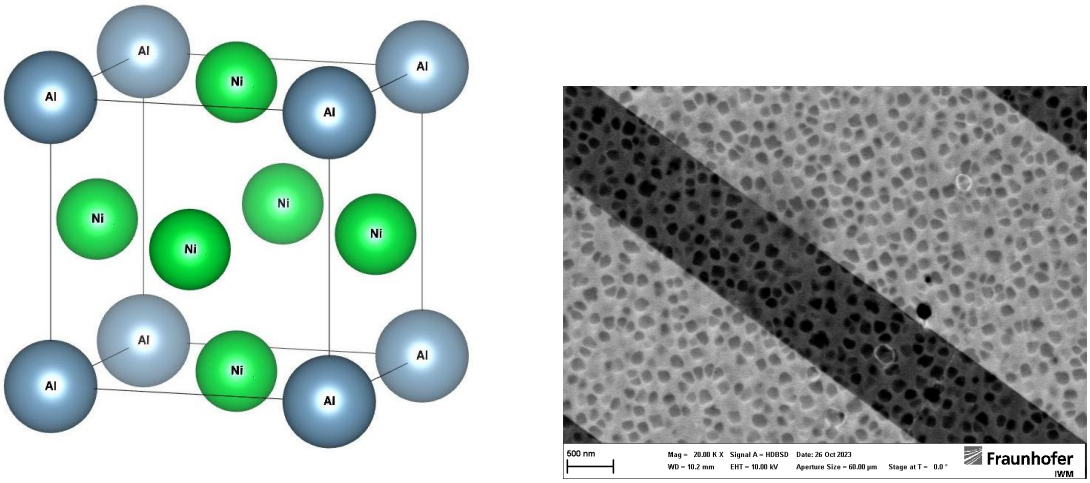

(a) (b)

Fig. 2.1 a) Schematic of the unit cell of the ordered Ni_3Al phase with aluminum atoms at the corners and nickel atoms at the faces; b) Backscattered electron image of the γ' precipitates across twin boundaries.

2.1.2 Alloying elements in Rene'88DT

The alloying elements in Rene'88DT can be divided into four groups, each of them playing a different role in the material. Some elements may more or less belong to both of the first two groups, providing solid solution strengthening of the matrix and the precipitate, however not to the same extent, as indicated in table 2.2 by the use of brackets. The elements of the first group preferentially partition into the FCC matrix, i.e., provide solid solution strengthening. Similar to the first group, γ' formers strengthen the precipitates in terms of increasing hardness, lowering the stacking fault energy (SFE), and raising the solvus temperature [5]. The third group, the carbide formers, form either primary (MC) or secondary carbides ($M_{23}C_6$, M_6C, M_7C_3), the latter form during the heat treatment out of primary ones and are located mainly at the GBs. The last group contains the grain boundary strengthening elements. The elements of the first group can be found in the periodic table in groups V, VI, and VII. Formers of γ' are located in groups III, IV, and V. Because some elements have a strengthening effect in both γ and γ', excess contents of these elements could induce precipitation and their limits need to be considered in the alloying process [5].

The alloying elements may have additional beneficial effects for the material, for instance a decrease of the stacking fault energy, as observed for cobalt and titanium. A lower SFE inhibits cross-slip of screw dislocations. Chromium is an important element for the resistance to oxidization and sulfidation by forming an oxide layer at the surface, especially relevant at higher temperatures [5]. Aluminum similarly improves the resistance to oxidation.

Table 2.2 Role of alloying elements for nickel-based alloys.

Element	γ former	$\gamma^{'}$ former	carbide former	GB element
Cobalt	x	(x)	-	-
Chromium	x	(x)	x	-
Molybdenum	x	(x)	x	-
Tungsten	x	(x)	x	-
Aluminum	(x)	x	-	-
Titanium	(x)	x	x	-
Niobium	(x)	x	-	-
Boron	-	-	-	x
Carbon	-	-	x	-
Zirconium	-	-	-	x

Boron and zirconium appear as equiaxed GB strengthening precipitates in the range of 0.1-0.5 µm, inhibiting the formation of Ni_3Ti (η),[3] inducing beneficial effects with respect to ductility and creep rupture strength [7]. Carbides can precipitate at GBs and have a pinning effect on such, hence improving creep strength as well [10].

2.2 Principles of fatigue life

Fatigue in materials refers to the phenomenon of damage generation through cyclic loads smaller than the ultimate tensile strength (UTS). This can lead to the initiation of cracks and eventually to the failure of a component/material. Within mechanical fatigue, an important metric is the ratio of the minimum of the stress amplitude divided by the maximum. This R-value distinguishes between solely compressive, tensile, or mixed stresses. For R=-1 (fully reversed) the mean stress equals zero and the minimum of the stress amplitude is equal to the maximum but of different sign [11]. The number of cycles a specimen can withstand until failure varies with the applied stress and three different sections in the S-N curve, i.e., the stress amplitude over the cycle number, are acknowledged; low-cycle (LCF), long-life (LLF), and high-cycle fatigue (HCF). The first one is characterized by high stresses in the range of the yield stress and few cycles causing plastic deformation in specimens before failing. The LLF section is situated between the LCF and the HCF and the corresponding cycle/stress range often varies. The LLF provides a statistical value for the number of cycles at a given stress until failure and is usually a straight line in a double logarithmic S-N curve [11]. The strain in the HCF regime is primarily elastic and a large part of the lifetime is spent in fatigue

[3] Eta phase with possibly negative effects on (notch) stress rupture properties, when in acicular shape [2].

crack growth. For certain materials, a pronounced fatigue limit (i.e. a stress value) exists, below which theoretically no failure occurs, even if the cycles approach infinity. This limit is usually in the range of $0.4-0.5\times$UTS for metallic materials [11], but it depends on the type of loading and the R-value. The UTS of Rene'88DT is approximately 1250 MPa [12].

The turbine disks in aerospace and power generation applications are exposed to a complex combination of thermomechanical loads. Extreme rotational speeds, temperatures close to $0.6\times T_m$ (with T_m being the melting point) and the associated oxidizing environment require nothing less than a "super"alloy [1]. A major prerequisite of aerospace alloys is their "damage tolerance". The ENSIP states, that "Damage tolerance is defined as the ability of the engine to resist failure due to the presence of flaws, cracks, or other damage for a specified period of unrepaired usage [3]." This means that the material presents a sufficiently high resistance against fatigue crack propagation. It ensures that despite cracks initiating at weak points in the material such as inclusions, pores/voids, scratches, and cracks from the manufacturing process, dents or cracks from the operation, propagation up to critical crack lengths does not occur in service. A sufficiently small crack propagation rate further ensures that formed cracks can be monitored in non-destructive inspection during service intervals and their successive growth predicted. The safety limit is the number of cycles/hours, until an initial crack—from aforementioned causes, that has a length below the detection limit—reaches the critical crack length, for which the component could fracture during loading. Therefore, the inspection interval is set as one-half the safety limit to provide a safety factor to account for process variability. Even when cracks below the critical length are present, the material's stability has to remain. The goal for the material developers is to further reduce FCGR and to extend the safety limit to reduce inspections. Visual representations of this process can be found in Ref. [3].

Recommendations for research on damage tolerance in Ref. [3] include trade studies on the material, design concepts, weight, performance, and cost. This work has been published nearly 40 years ago and state-of-the-art methods regarding materials design and simulation have changed incredibly. State-of-the-art methods include two- and three-dimensional microstructural investigations on all length scales, atomistic simulations, and machine learning algorithms. To further establish a correlation between microstructural features and critical failure indicators, a thorough understanding of fatigue crack initiation, crack propagation and the role of microstructural features and alloying elements therein is imperative [13, 14].

Efforts have been made to gain insights into the fatigue behavior and the often competing failure mechanisms of pure FCC metals such as copper and nickel [15, 16], solid solution-strengthened FCC nickel-based superalloys e.g., IN718 [12, 17], and precipitation-

strengthened FCC nickel-based superalloys e.g., Waspaloy [10], Rene'88DT [12–14, 18–22], Nimonic 80A [10], IN718 [12]. Some of these investigations are summarized in section 2.3. A multitude of factors dictate the properties and reliability of the superalloy Rene'88DT, as follows:

- The complex chemical composition with more than ten alloying elements, where many elements have multiple roles and various effects on the microstructure, the low- and high-temperature mechanical properties, the corrosion resistance and general stability of the material (see section 2.1.2).
- The powder metallurgy processing route does not eliminate all pores and inclusions from the matrix, but generally creates a highly uniform and homogenous microstructure without shrinkage pores, segregations or unwanted precipitates and therefore removes some common sites of fatigue crack initiation from the material [6, 13].
- The applied heat treatments and the associated fraction and shape of the γ' precipitates.
- Differences in fatigue life exist for different loads (axial, bending, etc.), different specimen shapes and specimen sizes, even for the same material [19, 23].
- The effect of operative temperature—maybe not as significant as for aluminum alloys and steels —but something that should not be neglected when comparing results of fatigue testing.

2.2.1 Dislocations, PSBs, and grain boundaries

Dislocations are linear, one-dimensional defects within the crystal structure and the main carriers for plastic deformation in metals. Dislocations are often categorized into two classes; edge and screw dislocations. Former is the termination of a crystallographic plane within a crystal (i.e. addition of an extra atomic plane in one half of the crystal), or the perpendicular displacement of the two sides following the cut of a crystallographic plane. A screw dislocation can be rationalized by fixing one end of the crystals and inducing a displacement of the two crystals along the dislocation line, creating a "step" [24]. Every dislocation can be characterized by two variables, the Burgers vector **b** and the line element **s**. The Burgers vector is equal to a displacement of the two crystal halves as introduced above. The line element can be defined as a tangential unit vector of the dislocation line. The Burgers vector **b** and the line element **s** are parallel for screw dislocations and perpendicular for edge dislocations [24]. Dislocations can be created as dislocation loops, for instance during plastic deformation. Thereby a shearing motion of two parts of the crystal along a crystallographic

plane will create two anti-parallel edge and screw dislocations, respectively. These dislocation loops can be observed in metallic materials only through transmission electron microscopy and can form into ladder structures when the screw dislocations annihilate through cross-slip [15, 24]. In a TEM brightfield image, individual dislocations and dislocation loops will appear as dark lines, because the associated distortion leads to a local fulfillment of Bragg's law and diffracts incoming beam electrons, therefore reducing the intensity on the screen. The cross-product of **s** x **b** defines the normal **m** of the glide/slip plane along which the dislocation moves. It is evident that screw locations have no particular slip planes, as of their parallel nature for the dislocation line and the Burgers vector, i.e., they have the ability to cross slip. To move a dislocation a shear stress larger than the Peierls stress τ_P is necessary on the slip plane:

$$\tau_P = \frac{2G}{1-\nu} \exp\left(-\frac{2\pi}{(1-\nu)}\frac{d}{b}\right) \tag{2.2}$$

The exponential relation between the Peierls stress, and the ratio of lattice spacing **d** and Burgers vector **b** results in minimum τ_P when their ratio becomes maximum, i.e., for densely packed planes. In a FCC material, like Rene'88DT, this is the case for $\{1\,1\,1\}$ planes and $\langle 1\,1\,0\rangle$ directions, because $d \propto (h^2+k^2+l^2)^{-1/2}$ and b=a/2$\langle 1\,1\,0\rangle$. This means that nearly all slip happens on one of the four $\{1\,1\,1\}$ planes and along one of the three $\langle 1\,1\,0\rangle$ directions, leading to a total of twelve slip systems. Which slip system will be activated is then a matter of Schmid factor (the locally resolved shear stress) [24].

When deformation occurs on the activated slip systems, slip bands will form on the same crystallographic planes. These slip steps are readily visible on polished metal surfaces after tensile tests or even after only one fatigue cycle [12]. Because these slip bands can form again on the surface even after they have been polished away, they were termed "persistent slip bands" (PSB) and were shown to be not merely a surface phenomenon, but had their origins in the bulk. Since slip is rarely fully reversible during cyclic loading—depending on the material—the slip bands can form more or less prominent surface markings known as intrusions or extrusions on the surface. Many models have attempted to explain the formation of intrusions and extrusions, but Watt's model (for fatigue in copper single crystals) appears most complete, when TEM observations are taken into account. The creation of extrusions/intrusions was explained by a combination of edge dislocation dipole loops and dislocations driving them to the surface. The underlying mechanisms for polycrystalline superalloys may be even more complicated [11, 15].

One of the main differences of polycrystalline materials is the presence of GBs. Grain boundaries are three-dimensional defects, which separate volumes of the same phase (chem-

istry) but of different crystallographic orientation. However, they are most often only observed in two dimensions, due to the limited tomographic resources and associated experimental difficulties using TEM, FIB-SEM, or DCT [24]. In a two-dimensional section the rotation angle θ corresponds to the tilt of the lattices of the two adjacent grains. LAGBs ($\theta \leq 15$) can be explained by the accommodation of individual dislocations forming the boundary. HAGBs ($\theta > 15$), however, cannot be explained by the dislocation model of LAGBs, because the grain boundary energy does not change with increasing rotation angle and the dislocation model fails, because else the cores would overlap. In this regard, the coincidence sites are introduced. It states that due to the minimization of free energy, there are always atoms in the grain boundary that coincide with ideal positions from both grains. These sites form a coincidence site lattice (CSL). Because of the periodicity of both crystal lattices, the CSL is also periodic. The elementary cell is larger than the elementary cell of the crystal lattice for rotation angles >0 °. To define the density of coincidence sites, a parameter Σ is introduced:

$$\Sigma = \frac{\text{volume elementary cell of CSL}}{\text{volume elementary cell of crystal lattice}} \tag{2.3}$$

A highly ordered GB, such as a LAGB, will have a Σ value of Σ=1. Twin boundaries have per definitionem Σ=3 and are sometimes referred to in the literature as Σ3 boundaries. Real grain boundaries do get a lot more complicated, so for rotations other than those with perfect alignment of the atomic positions at the GB, additional GB dislocations need to be introduced to accommodate the misorientation. Further details can be found in chapter 3.4 of Ref. [24].

2.2.2 Schmid's law

In 1935 Erich Schmid and his colleague Walter Boas of the University of Fribourg, Switzerland, published a book titled "Kristallplastizität mit besonderer Berücksichtigung der Metalle", which was translated into English in 1950 under the title "Plasticity of Crystals with special reference to metals". Therein they describe many theories related to crystals, their glide, shear, and tensile strength. They underpin their theoretical expressions often with experiments on crystals and images thereof. Especially interesting is their introduction to the "Critical shear stress law", which was later named after Erich Schmid. It states that in a common uniaxial tensile test, the shear stress will be different on differently oriented glide planes and therefore, dislocation motion (and material yield) is only possible on certain planes. Hence, the orientation of the crystal lattice with respect to the imposed uniaxial load, plays an important role for the yield point. They found that a hexagonal magnesium crystal

oriented for high strength had a 40-fold higher yield point than a weaker crystal. For cubic crystal structures, the effects are smaller but not negligible [25]. Schmid's law relates the applied uniaxial load to the induced shear stress on the slip systems. The shear stress (S_0) is affected by the two angles the tensile stress axis spans with the glide plane (χ_0) and the slip direction of the plane (λ_0):

$$S_0 = \sigma * \sin\chi_0 * \cos\lambda_0 \tag{2.4}$$

which was later revised to:

$$\tau = \sigma * \cos\kappa * \cos\lambda = m\sigma \tag{2.5}$$

Where κ or λ represent the angles between the tensile loading direction and the normal vector of the glide plane or the slip direction, respectively [24]. With this approach we can define a maximum value for m, which will be referred to as Schmid factor or SF throughout this thesis; m reaches a maximum of 0.5 for $\chi_0 = \lambda_0 = 45$, because $\sin\frac{\pi}{4} = \cos\frac{\pi}{4} = 0.707$.

Plastic deformation will initiate along those slip systems which first reach a critical shear stress (τ_{CRSS}, also known as "critical resolved shear stress"). This dependence can be plotted for all slip systems–once the orientation is known–in stereographic projections of the cubic crystal with contour lines of equal SF, as in Ref. [24], chapter 6.4.1. Schmid's law was originally designed for quasi-static tensile tests, however, it can be applied to cyclic tests as well if the load can be translated to an axial tensile load. The shear stress in surface grains with high Schmid factor will surpass that of other grains with lower SF and therefore the motion of dislocations will be confined to the higher stressed planes.

This connection between highly strained regions in tensile tests and fatigue crack initiation has been made by Stinville et al. for Rene'88DT [13]. In tensile tests they identified that the highest strain localizations occurred in certain parent-twin configurations; the parent and the twin grain both had to have a high SF and the difference in elastic modulus in the two was greater than a specific threshold. When they later investigated such regions in fully-reversed low-cycle fatigue tests, they found that these regions were favorable for fatigue crack initiation [13].

2.2.3 Crack initiation and crack propagation

The initiation of microcracks has been linked to the formation of intrusions and extrusions by Mughrabi [15]. During cyclic loading, the dislocations travel to the surface on crystallographic planes inclined approx. 45 ° to the external loading, due to the resolved shear stresses. The surface roughening created by the persistent slip bands and the associated sharp notches cause stress concentrations and were established as a prerequisite for the initiation of fatigue

cracks. Plastic strains greater than the average plastic strains have been measured at the interface of the PSBs and the matrix [15, 26]. This applies to macroscopic and microscopic fatigue (tests) on ductile FCC metals.

Tanaka, Mura, and Venkataraman explain the crack formation by two planes, which form during the slip. Positive dislocations form on plane one during tensile loading, while negative dislocations form on plane two during compressive loading. These two planes exist closely spaced within the same slip band. With every cycle dislocations pile up at the GBs on both layers due to the increased stresses of the dislocations on the respective opposite layer (cyclic slip irreversibility). This interfacial dislocation pile-up can become so great that it is not energetically favorable anymore due to the increased elastic strain energy and crack occurs [11, 27].

For Rene'88DT, fatigue crack initiation is known to occur often parallel to Σ3 TBs. But only parent-twin constellations, where a slip system with a high SF is parallel to the TB, initiate cracks. A possible reason is the motion of dislocations, that are created at low stresses along these TBs. Due to the coherency of the TB, they are able to travel on the activated slip system, creating strain, until they reach the GB on either side, causing a dislocation pile-up. When slip does occur across the TB, the recorded strain localization is considerably lower. Additionally, shear was measured to be up to three times as high at parallel slip system-TB occasions as at transgranular slip bands. Because the γ' precipitates can be easily sheared, local softening and hence preferred slip along narrow bands occurs. The precipitates are also expected to be the reason for the high amounts of extruded material at cracks. In which grain the crack initiates, is linked to elastic heterogeneity, that is a necessary consequence for parent-twin grain structures with identical activated slip systems [13, 20, 21].

Considering 3D structures, another factor may influence the crack initiation in superalloys: triple junctions. They describe the conjunction of three grains in one point within the material. Slip bands have been found to connect to triple junctions in many occasions and high lattice rotations were also observed at such. Lattice rotations were also shown to contribute to the irreversibility of intragranular lattice misorientation [28]. Furthermore, the slip bands with the highest intensity have often been linked to the presence of both twin boundaries and triple junctions [17].

In investigations with 3D crystal plasticity extended finite element modeling (3D CP-XFEM), Zhang and Dunne [21] confirmed the importance of elastic anisotropy across the TB for cracks planar and parallel to the $(1\,1\,1)$ TB. Additionally, they evaluated stress concentrations and were able to show increased values for the $60\,^{\circ}$ twist angle at TBs, once more supporting crack initiation and high propagation rates [21].

The nomenclature for cracks of different lengths in this thesis was adopted from Bataille and Magnin [29]. They distinguish between four types of cracks based on the number of grain boundaries they overcome for grains of average size. Hence, a crack may still be of a lower/higher order if the grains in which it propagated are very small/large, respectively. Generally, the classification is as follows; type I cracks are confined to one single grain and are here broadly referred to as microcracks, while type II cracks may spread across three grains. Type III and type IV cracks have already propagated across less and more than ten grains, respectively.

2.3 Fatigue in Rene'88DT: State-of-the-art

Since the material's introduction in 1992, it has been subject to numerous investigations and there is still a high interest in understanding the mechanisms and microstructural features involved in the fatigue behavior of Rene'88DT. Current efforts involve the development of mechanism-driven predictive models, which can relate descriptors of the polycrystalline microstructure to the resulting material's properties and crack initiation tendencies. The computational methods used for modeling require accurate state variables, i.e., local plastic strains at locations where cracks are likely to initiate. Without precise values, the successful development of mechanics-based models for the nucleation of fatigue cracks is not possible [14].

In the following subsections, the most important findings of the relevant literature are summarized and in chapter 6 the results, that were obtained during this master's thesis, are compared to this previous work.

2.3.1 Related works

In this section, the results from four fundamental investigations into fatigue of Rene'88DT are summarized and compared. The oldest paper in this regard is titled "Microstructural extremes and the transition from fatigue crack initiation to small crack growth in a polycrystalline nickel-base superalloy" from Miao et al. [30] in 2012. The authors summarize their work with

> This present study investigates the effects of microstructure, especially the role of "microstructural neighborhoods", on cyclic plastic deformation, fatigue crack initiation and early small crack propagation on René 88 DT at room temperature.

This focused on microcrack initiation sites using EBSD analysis, the characterization of the growth of short cracks, and the investigation of TEM samples. They employed uniaxial,

fully-reversed ultrasonic fatigue testing on cylindrical specimens at room temperature. The frequency used on the Rene'88DT samples was close to 20 kHz. The samples were investigated in the long-life fatigue and high-cycle fatigue regime with cyclic stress amplitudes ranging from 460 to 720 MPa. All of the propagating cracks started at the surface of the specimens. Their initiation was linked to twin boundaries in large grains and were parallel to the TB with a slight offset. This points to the fact, that the elimination of larger-than-average grains may be beneficial to improve the fatigue life of Rene'88DT. A unique finding was that transgranular fatigue crack propagation across GBs was limited to neighboring grains with a misorientation of less than 20 °. Transgranular cracks were found to arrest for larger misorientation angles. When plotting grains where crack initiation occurs in an inverse pole figure with SF contours, it is apparent that almost all of the crack initiation sites are associated with a high SF and therefore a preference for dislocation slip. The elastic incompatibility at TBs was suggested to be the main reason for the strain localization and subsequent crack initiation.

Stinville et al. [20] published a combined grain scale elastic-plastic criterion for the identification of fatigue crack initiation sites, which involved low-cycle and very-high-cycle fatigue crack initiation experiments, complemented by ex-situ SEM-DIC on fatigued specimens, crack density and distribution analysis. Cylindrical push-pull tests in an axial setup were utilized. They mention an average lifetime of 65,000 cycles at 760 MPa stress amplitude at room temperature, and a frequency of 1 Hz.

The testing routine for the LCF regime included EBSD images before testing, and after interrupted fatigue tests at the mentioned stress amplitude, sub-grain SEM-DIC image acquisition before, during and after testing[4] and crack density measurements with SEM. Because EBSD imaging requires a flat surface, the gauge section of the specimens was flattened on opposite sides along an area of 2.5×8 mm. This ROI was analyzed with respect to strain partitioning and its link to microstructural features. For DIC the researchers decided to utilize a Fe(III) chloride etchant to generate the desired speckle pattern, which does not compromise EBSD analyses, as an application of gold particles might do.

The Open-DIC software with a DIC subset size of 27×27 pixels and 17 pixels between subsets was employed. The zero-normalized cross-correlation was used and this enables an independence of subsets from neighbors. They claim a resolution of about 0.1 pixel, equal to 6.2 nm for the displacement. Subsequently, the in-plane strains ε_{xx}, ε_{yy} and ε_{xy} were determined by introduction of four Gauss bilinear interpolation points for each element.

[4] After testing refers to specimen failure.

The results of the LCF investigation were as follows; cracks initiated always near Σ3 TBs on the active slip plane,[5] which was parallel to the TB. They observed the initiation of type I cracks after 20 % of the lifetime, propagating only 40 % of the time into a higher-order crack. Crack propagation was not related to the microstructure in their findings, but initiation was. Utilizing DIC, they found localized (compressive) strains after only one cycle, compressive and tensile strains after 15 and 45% lifetime, close to the crack initiation sites and at a parallel offset of 0.8 µm from the TB. The crack location was a TB, where twin and parent grain were oriented for high shear (SF=0.493) and their activated slip planes were parallel. They were able to quantify the strains (ε_{xx}) and the peaks at the future crack site next to a twin boundary were as follows: -3.5 % after one cycle; -2 % and +3 % after 15 % lifetime; -4 % and +12 % after 45 % lifetime. This shows that compressive strains predominate the early phase of fatigue but do not significantly increase with a higher number of cycles, while tensile strains develop later, but increase very quickly. Failure could therefore be linked to the building up of tensile strains in the material.

Stinville et al. [13] published another paper in which they supplemented the previous results in cyclic loading with DIC analyses of tensile tests of Rene'88DT. Strain localizations were observed near TBs and increased with high elastic modulus mismatch between the twin and the parent grain, but also for cases where the twin plane was parallel to an activated slip plane with the highest SF. They observed that activated slip planes parallel to TBs have the same SF as the ones in the parent grain. Therefore a high SF in both can be present. A scatter plot displaying the elastic modulus difference plotted versus the maximum SF clearly indicates that strain localization preferentially occurs in grains which maximized this combination, especially for SF greater than 0.45. For example, a grain with ΔE of approximately 135 GPa and SF of 0.459 and another grain with ΔE of approximately 55 GPa and SF of 0.493. This clearly shows, that both values are important for the strain localization in tensile tests.

The most similar investigation by Alam et al. [18] involved a bending resonance fatigue setup that was essentially the same as in this thesis, except that they employed a different control procedure and no in-situ darkfield camera imaging was applied. They tested their samples with a maximum bending stress of 80 MPa and they reported multiple slip bands within grains containing twins and even microcracks in large grains, within a few hundred thousand cycles. The observed slip bands were found on the activated slip system in grains that did not initiate a crack but had a high SF. They were not parallel to a TB and in one instance even penetrated one. In one EBSD scan, the authors argue that multiple dark lines formed parallel to each other and penetrated the—rather narrow—twin. Microcracks started

[5] Slip plane with the highest resolved shear stress.

parallel to (but not directly at) twin boundaries in grains larger than the average grain size of around 20 µm. They associated the formation of cracks with locally high shear stress due to a high dislocation density and shearing of γ' precipitates. Additionally, the dislocations in the slip bands are not hindered in parallel gliding, as it doesn't interfere with the TB. The glide is enhanced by the local stress concentration due to elastic incompatibility across the TB. The larger the grain, the longer the twin (statistically) and the greater the free glide length, again leading to higher stresses. It is mentioned, that the multitude of γ' precipitates sheared on the glide plane can increase local strains and have an effect on microcracks, but no reasoning is given.

In summary, large grains (i.e. longer twin boundary), high Schmid factor in twin and parent grain, and a certain elastic modulus mismatch across the twin boundary are necessary to initiate cracks parallel to Σ3 TBs. The propagation of cracks may be inhibited across grain boundaries with more than 20 ° misorientation.

Chapter 3

Experimental methods

Investigating the development of intragranular strains, caused by local motion and accumulation of dislocations, often concentrated on a few extremely fine glide planes, requires the usage of undeformed specimens. The surface ought to be as flat and free of deformation as possible to enable a high pattern quality for EBSD analysis and HRDIC, both done with a scanning electron microscope. Additionally, in fatigue tests, cracks are very prone to initiate at small surface defects, such as scratches, sharp edges or (larger) pores. The initiation of cracks at (non-metallic) inclusions due to elasticity mismatch and incoherence can be overlooked in this regard, as none were evident in the mesoscale samples. Moreover, some limitations were made to the geometry because of the bending resonance fatigue setup: A specimen design with a tapered bending beam is selected to obtain a rather homogeneous stress state over a region of interest, which fits into the camera field of view. Thickness is limited to 250 µm or less to keep the f_{res} below 1,500 Hz and the edges in the tapered section need to be rounded to ensure that cracks do not initiate there. All these factors had to be taken into account during specimen preparation.

In order to evaluate the microstructure of the samples and its relation to crack initiation (compare with section 2.3), detailed imaging of the sample surfaces is necessary. The final specimens were evaluated before and after the fatigue testing to identify where microcracks had formed, where strain localizations appeared near cracks (HRDIC) and how this fatigue damage is connected to the microstructure. When referring to the microstructure, important properties to be analyzed were the grain size, density of twin boundaries, crystallographic orientation, elastic modulus in loading direction, grain boundary misorientation angle, and properties which relate crystallographic features of a grain with mechanical loading, i.e., micromechanical variables such as the Schmid factor. Other properties including anisotropy, chemical/phase composition, hardness, and density were not subject of this investigation,

as they were considered to be non-existent or uniform across the material and have been recorded in the past.

To obtain the necessary data, the workflow (fig. 3.1) included an EBSD scan, a high-definition backscattered electron detection image (HDBSD) (both about $500 \times 650\,\mu m$ in size), and additional high magnification images of potential crack initiating grains. After the subsequent fatigue test, both sides of the specimen were imaged again, without the EBSD scan, since no major changes of the grain size or crystallography are expected to occur under high-cycle fatigue loading. The images were then stitched together using ImageJ to ensure a high resolution of the entire ROI.

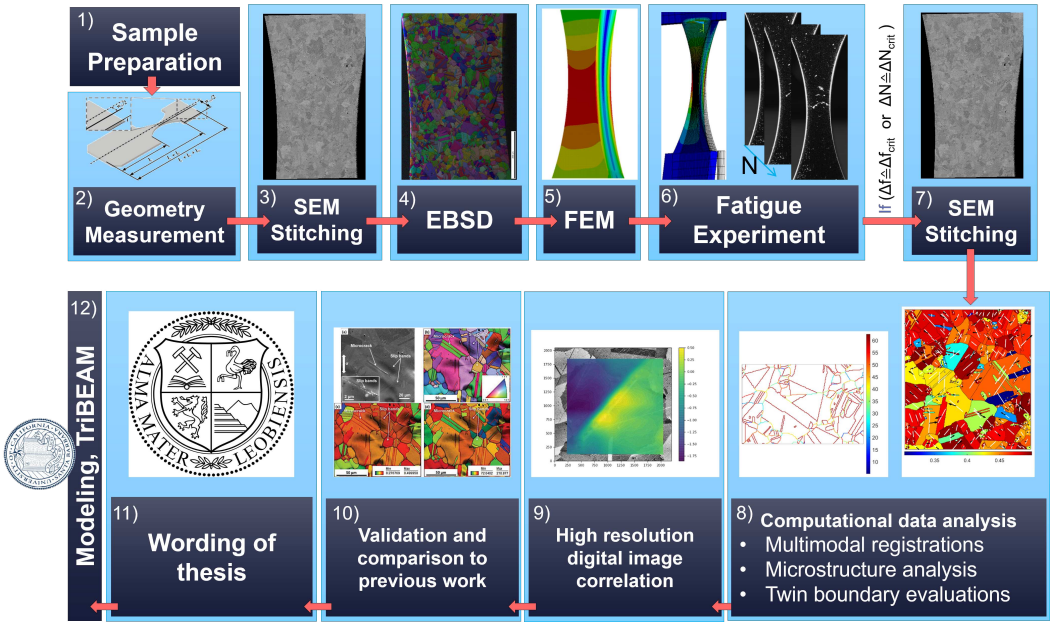

Fig. 3.1 The workflow for this master's thesis (1-11) and consecutive investigations with a femtosecond laser and 3D EBSD (12).

3.1 Specimen preparation

3.1.1 Grinding and polishing

The bending resonance fatigue specimens were extracted from the clamping area of macroscale cylindrical fatigue specimens, that were previously tested in another research group. As stated in the standard for fatigue testing DIN 50100, the clamping section experiences no stresses during the fatigue test and is therefore considered as undeformed [31]. The cylinders were subsequently sectioned into small sheets of about 650 µm thickness with wire electrical

discharge machining (WEDM). Out of each sheet, one specimen was cut. The macroscale specimens may have been machined from an actual turbine disk, but their position therein is not relevant, because of the powder metallurgy process and its homogeneity. WEDM is a very accurate machining process (kerf as small as 20 µm) and low residual stress introduction into the material.

The desired thickness of the sheets was 650 µm and reaching this consistently should not be a problem with WEDM, but the samples delivered were found to have thicknesses of 590-650 µm. This posed a first challenge for the grinding process. The grinding process included the mounting of the bending resonance fatigue samples onto a steel cylinder because they would otherwise be too delicate to be ground by hand. This involved the heating of the cylinders to about 150 °C, then applying a thin film of adhesive of appropriate thickness (Crystalbond 509 adhesive), which needed some practice to make sure that no specimen edges were exposed. This could damage the polishing cloths and in turn the samples themselves. The application of excess adhesive, however, would let it flow over the specimen and needed to be removed before grinding, otherwise the entire surface would be skewed. Once the samples were embedded in the hot glue, the cylinder was put into a pneumatic press made of copper. The copper ensured a high heat conductivity while the samples were held down with a contact pressure of 3 bars and cooled in a water bath. After about three minutes the cylinder with the samples was taken out of the press and the adhesive was left to cure for about 12 hours.

After curing, the mounted samples underwent grinding with the 320 SiC paper for about 40 seconds to remove about 120 µm of the surface, then a fine polishing with the 1200 paper for one minute to remove another 75 µm and get the samples ready for polishing (see table 3.1). Thereby the thickness of the samples was reduced to 250 µm and slightly below that. But with this aforementioned variation in thickness, one sample would have been 190 while the other was 250 µm. Therefore, the samples' thickness had to be measured after the grinding and polishing on the first side and samples with a similar thickness were mounted onto the same cylinders to ensure a small deviation in thickness. The polishing routine used is standard for nickel-based superalloys [32] and culminated in a good surface quality according to the SEM and EBSD measurements. However, because the electropolishing (section 3.1.2) was found to decrease the surface quality substantially, an additional step of OPS-polishing was added after the initial polishing. For the OPS-polishing step, the samples were mounted again onto the cylinders, being more difficult this time because of their already reduced thickness.

Table 3.1 Grinding and polishing steps. Polishing with MD-Chem was the only one where the platen and the head rotated in opposite directions.

Step	Paper/Cloth	Abrasive	Time	Force [N]
Grinding	P320 grit SiC	-	40 s	30
Grinding	P600 grit SiC	-	60 s	30
Polishing	TexMet	9 µm diamond suspension	8 min	15
Polishing	MD-Dac	3 µm diamond suspension	5 min	15
Polishing	MD-Nap	1 µm diamond suspension	5 min	15
Polishing	MD-Chem	0.05 µm alumina suspension	15 min	15

3.1.2 Electropolishing

After the first preliminary bending resonance fatigue test, it was evident, that cracks would initiate at the sharp edges of the sample. The sidewall was still in the original state from the WEDM and hence rather rough. But because it was necessary for the investigation that the microcracks initiate in the middle of the samples, due to microstructural conditions, and not at the edges, due to stress concentrations, a step of electropolishing was added after the 1 µm fine polishing. The electropolishing setup used was once developed for exactly this type of specimen, but after not being used for multiple years, the LabVIEW program did not work anymore, as some files were missing. Hence, a thorough restoration, which took weeks and included many failed attempts, was necessary to get the setup back up and running. A different setup from Struers, the Lectropol-5, was also tried but failed because the samples were so thin that the electrode that contacts the material was unable to hold the thin samples in place whilst being exposed to the electrolyte stream, effectively causing ill-defined polishing states and poor reproducibility. Finally, the samples were electropolished using Electrolyte A2 from Struers, which is a two-part mixture containing perchloric acid, ethanol, 2-butoxyethanol, and water. A voltage of 16 volts was applied for 8 seconds to the sample. Usually, the right voltage for polishing is obtained from the current density over the electrode potential diagram (polarization curve). The diagram can be divided into four sections of increasing applied voltage; etching, passivation, polishing, and pitting/gas formation. Typically, the polishing region has a plateau, i.e., a constant current density despite increasing voltage. Kinetically, the passivated layer formed on the surface transports diffused anions from the metal's surface to the surrounding electrolyte [33]. Beyond the polishing regime, the current will increase again and break down the passivated layer, causing degassing and pores on the sample surface. This polarization curve can be mapped out with an inherent program on the Lectropol. However, this was not possible for the bending

resonance fatigue specimens, as they showed nothing but a linearly increasing current density with no sign of a plateau. Therefore, the only option was to find the polishing voltage range manually. With a trial and error procedure, steps were made in the right direction, by trying different voltages, polishing times, and flow speeds. Because of the custom setup, it was necessary to control the flow around the sample manually, to ensure new electrolyte was supplied to the polishing interface at all times. The glass cylinder was standing on top of a magnetic rotating device and in the cylinder was a common agitator rotating at different speeds. At first, the rotating speed was rather high, causing grooves on the samples, but an ideal speed was determined at 140 rpm. The electrolyte was additionally cooled with cold water to ensure a constant temperature, as usually an increase due to the polishing current occurs and polishing would not work above a certain electrolyte temperature. The formation of dimples on the surfaces of samples electropolished early in the parameter-finding process was removed by slightly increasing the polishing time and further decreasing the flow speed from 300 to 140 rpm. Images of this device and the custom-made u-shaped electrode can be found in the appendix (fig. A.7, fig. A.8).

The electropolishing setup was controlled by a custom LabVIEW program from former investigations and had to be adapted for this study, as some files were missing and had to be restored with the help of programming experts. After the input polishing time, the voltage would turn off automatically and the sample could be removed. The samples were subsequently cleaned in two steps; (i) a dip into acetone to remove residual electrolyte from the surface and (ii) a prolonged submersion in ethanol to remove the acetone. This combination was found to yield the best results and inhibit unintended etching of the sample. After the ethanol bath, the samples were dried with pressurized nitrogen. In contrast, drying the ethanol with hot air left stains on the polished samples.

In literature, it was mentioned that electropolished surfaces would yield superior EBSD pattern quality compared to chemo-mechanically (OPS) polished surfaces, as it introduces no deformation [33]. This was however not the case in our study. A sample was analyzed with EBSD after electropolishing; the image quality and confidence index[1] were detrimentally low. Thus, the sample was subjected to an additional step of OPS-polishing for 15 minutes to achieve a better surface quality. However, mounting, polishing, and subsequently cleaning the sample again could introduce fine scratches and slight deformation of the sample surface. This was indeed the case and was especially obvious using the backscatter detector, which has a higher depth sensitivity than SE2. Nevertheless, these minor scratches were not found to influence the bending resonance fatigue, because cracks did not initiate at the scratches nor follow them during crack propagation.

[1] See section 5.1 for explanations.

3.2 SEM imaging

For this project, the imaging and analysis of the specimen surface was particularly important to establish correlations between initiation sites of microcracks and the microstructure. The ultimate goal, far beyond this thesis, ought to be the enhancement of models to predict crack initiation and to alter the microstructure to provide a superior fatigue resistance. Therefore many tests were conducted to find the best imaging parameters which can be summarized as follows:

The backscattered electrons were found to be the best option for recording surface cracks and DIC. For microstructure characterization, EBSD was used and the OPS-polished samples gave the best image quality. In the following two subsections, both methods are described in detail.

3.2.1 Backscattered electron detector (BSD)

The Zeiss Sense BSD is located below the pole piece and enables the recording of images with high orientation contrast. Backscattered electrons are primary electrons that leave the sample again after one or multiple scattering events. Their fraction is described by the BSE coefficient η and increases with increasing atomic number Z, but not with increasing voltage, as one may intuitively think. The BSE signal can yield information about the sample's topography, chemical composition, mass thickness, and crystallography. These electrons can escape from up to 150 nm beneath the surface for pure copper and 10 kV, as compared to less than 10 nm for secondary electrons, which are not the same electrons as the primary electrons. This results in greater contrast between different grains or between the γ' precipitates and the matrix as can be seen in fig. 3.2 [34].

3.2.2 Electron backscatter diffraction and data analysis

Electron backscatter diffraction (EBSD) adds a crystallographic analysis tool to a common SEM. Grain orientation, phase identification, and microtexture in polycrystalline materials are just some of the aspects that can be explored in a quantitative manner. The surface of the tilted sample (about 70 ° relative to the incident beam) is scanned with a particular step size. The electrons of the beam are diffracted in about 20 nm depth beneath the surface when Bragg's law is fulfilled:

$$n * \lambda = 2 * d_{hkl} * sin\theta_{hkl} \tag{3.1}$$

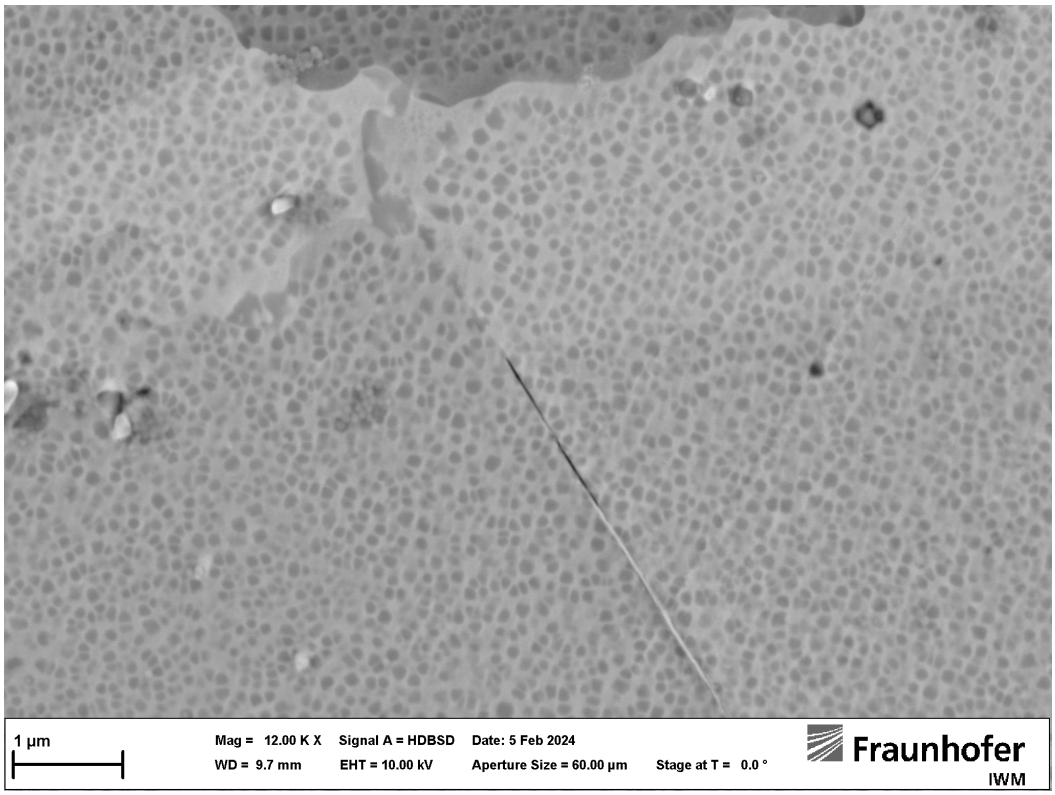

Fig. 3.2 BSD image showing the arrest of a crack near a triple junction with a depleted zone of γ' precipitates.

Where n is the order of diffraction, θ_{hkl} the Bragg angle, λ the wavelength depending on the acceleration voltage, and d_{hkl} is equal to the interplanar spacing. The diffracted electrons will form two cones in the direction of the geometric projection of the plane onto the phosphorus screen (EBSD detector), which is located about 2 cm from the sample. The two cones with opening angles close to 180° are visible as (nearly) parallel lines, brighter than the background, and are commonly referred to as Kikuchi lines/patterns. These lines are subsequently analyzed by a computer program and, since they are connected to the crystal orientation and crystal structure (spacegroup of nickel in this case), the orientation of the grain (crystal reference frame) with respect to the sample coordinate frame can be determined. This indexing provides the foundation for evaluating the Schmid factor or the elastic modulus along the loading direction. For the calculation of the SF, the angles between the slip plane normal and the slip direction with respect to the loading direction are required (see section 2.2.2) and can be calculated once the orientation of the grain (and with it the orientation of the slip systems) within the specimen is determined.

3.3 Bending resonance fatigue

Bending resonance fatigue testing is a particularly interesting tool to analyze fatigue damage and related microstructural effects, because:

1. The maximum stress is located on the surface of the material (at least in this setup), allowing direct correlation of the microstructure with the resulting damage evolution before a fatal/large crack becomes evident. Such early fatigue damage may include persistent slip bands, extrusions or protrusions (see section 2.2.3). In axial setups, the forceful opening of a crack is often necessary to observe the early stages of crack initiation and propagation. Additionally, if cracks start at inclusions inside of the specimen they may not even be visible on the surface. That this does not have to be the case was shown by Stinville et al. in 2017 [13]. They were in fact able to locate small cracks on the surface of a specimen tested at R=-1 in an axial setup, but could not determine the exact time (i.e. number of cycles), at which they became visible.

   The setup used in this thesis is coupled with a camera that acquires dark-field images in which cracks (and larger extrusions) will be visible as soon as they emerge on the surface (live) due to the scattering of light at the surface defect. An image is taken the moment the specimen has returned to its initial position, i.e., at zero displacement. Unfortunately, this is not possible after every single cycle because the exposure time of the camera is much longer than the time for one fatigue cycle. Thus, an image is taken after a couple of cycles. During longer tests (e.g., VHCF) pictures are taken about every 100 seconds as damage evolves slowly. For fatigue crack investigations, this means that you can track the initiation and propagation of a type I crack into a crack of higher order along with the number of cycles and assess the site of the nucleation by additional electron backscatter diffraction.

2. The unique setup of the bending resonance fatigue enables the interruption of the test (automatically) when a certain criterion is reached. These criteria include a relative or absolute change in the resonance frequency, the reaching of a specified number of cycles, or the local observation of cracks on the surface in the darkfield image due to increased pixel intensity. The darkfield image shows only one side, however a symmetrical stress amplitude is present [35].

3. In conventional macroscopic setups, testing frequencies are generally lower and therefore tests in the HCF and VHCF regime can be time-consuming. Bending resonance

fatigue testing, however, allows for frequencies of more than 1,000 Hz and will therefore only need about one and a half hours to reach ten million cycles. The data has to be considered carefully, because, as Shyam et al. [36] point out, fatigue lifetime in ultrasonic testing will be shorter than in conventional testing at significantly lower frequencies. Zhao et al. [23] claim in a much later study, that frequency effects were much greater in the range from 0.001 to 10 Hz than they were between 10 and 20,000 Hz. While these are important factors to consider for engineers determining the inspection and service intervals for components, it is less relevant to this thesis, because the focus is rather on the location of emerging damage in the microstructure than the amount of time that passed until then.

4. The provided material contained only three pieces of already fatigued macroscopic cylindrical specimens from push-pull axial setups. The only viable extraction could therefore be made from the clamping regions, about 30 mm long and 10 mm in diameter, leaving only meso- or microscale mechanical testing as an option. Such small-scale investigations can also include thin films, or to determine local fatigue properties in gradient materials, e.g., the testing of the fused zone in a weld. There is however also some critique and open questions about small-scale investigations. This includes the size of the samples and the associated inaccurate representation of defect distribution and microstructural features. This is known as the statistical size effect, wherein the number of defects within a specimen statistically decreases with decreasing specimen size. It could be argued, that this is less pronounced for Rene'88DT due to the powder metallurgy route and the corresponding homogeneous microstructure [22].

5. Furthermore the disk of a combustion turbine is rotating at such high speeds that essentially low-amplitude vibration is always a side-effect due to disturbances. Vibrations due to the difference in gas dynamic loads are also commonly observed [4]. The bending resonance fatigue testing makes it easy to test the specimens at high frequencies and mimic the stress of the vibration occurring in the real turbines [37].

6. Although damage may not yet be visible on the surface, it can be recognized by a change of the resonance frequency. The resonance frequency (f_{res}[2], equal to the frequency at which the specimen is tested) is a function of the material's elastic modulus, mass, and the geometry of the specimen and an estimate is determined through a modal analysis in the finite element (FE) analysis program called ANSYS (see fig. 3.3b). The mathematical expressions for the calculation can be found in the publication of

[2] Damping is not considered here.

Straub et al. [16]. In the paper, a relative frequency change ($\Delta f / f_{res,initial}$) of about -1x10^{-3} corresponded to the initiation of cracks. The experimental determination of f_{res} is done through a sweep from a slightly lower to a slightly higher frequency than f_{res}. In conventional tests, the occurrence of microcracks in comparatively larger specimens could not be detected, but in this much smaller volume, it is possible due to the much greater signal-to-noise ratio [16].

The experimental setup in fig. 3.3a uses two piezo actuators that excite the specimen in the clamping region and trigger the bending due to the inertial forces of the mass at the lower, free-swinging end. The actuators are able to ensure sub-millisecond response time for actuation in the kHz regime. They offer a bandwidth of up to 5 kHz and high-resolution position sensors for linearity to 0.01 %. The deflection of the the mass is measured by a laser positioned in front of the sample and determines the displacement amplitude which is then translated into a stress amplitude. The polished surface of the sample ensures proper reflection of the laser beam onto the position-sensitive device. The connected LabView program and the utilized field programmable gate array digitize the analog data from eight inputs and are able to stop the excitation in milliseconds when a set stop criterion is met in the program (e.g., absolute frequency change of 10 Hz). For further reading about the calculation of the stress, how the area detector works in detail and potential errors of the setup, the reader is referred to Ref. [16].

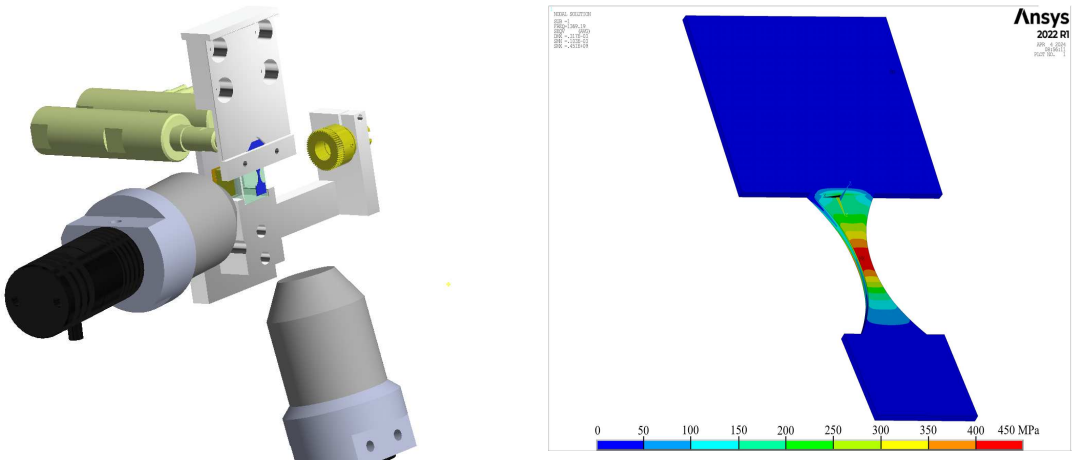

(a) (b)

Fig. 3.3 a) Model of the bending resonance fatigue setup with the piezo actuators in khaki, the specimen in blue and the LEDs left and bottom (provided by Durmaz et al. [35]); b) FE simulation showing the distribution of von Mises stress for the maximum deflection ($\widehat{=}$ 1.53 V) for specimen AZI-1105-A-BR.

3.3.1 Finite Element Simulation

The amplitude of the piezo actuators, corresponding to a certain stress on the surface of the fatigue specimen, was calculated using a continuum finite element modal analysis in ANSYS with a code from Durmaz et al. [35]. The code utilizes the geometry of the specimen with user input for the minimum width and thickness of the tailored section, the height and width of the mass section, and the elastic modulus and Poisson's ratio to generate a SOLID 185 3-D model with eight nodes having three degrees of freedom at each node. This type of element ensures smooth transitions between differently meshed volumes. In this case, the mass section and the gripping section have a single element along the thickness, while the tailored section has two. The following simulations calculate the eigenfrequency of the sample[3] and the voltage necessary to induce the desired bending, which is controlled by a laser and a position-sensitive device. The reflected beam will be registered on the area detector with a certain vertical offset–corresponding to a change in rotation angle for angles greater than 0 °. The specimens' f_{res} were in the range of 1030-1520 Hz and the voltage was around 1.3 V.

3.3.2 Bending resonance test

The tests were conducted using the setup of Durmaz et al. [35] following the efforts of Straub et al. [16] with the addition of bidirectional stroboscope illumination and image acquisition to track crack initiation and propagation, schematically depicted in fig. 3.3a. Overall, seven fully reversed bending resonance fatigue tests were conducted during this thesis. The specimen numbering system was devised during this thesis necessitated by the multiple top-down extractions until reaching the final mesoscale specimen. The first term is universal for all specimens and is an internal project numbering "AZI", where "AZJ" would be the succeeding project. The four numbers describe the three hierarchies of components: the first figure (in the range of 1...3) is the macroscopic fatigue specimen, a total of three was extracted from a turbine disk at an unknown location. The second figure (in the range of 1...2) stands for the cylinders that were extracted from the clamping region on either side of the cylindrical macroscopic specimens. From each cylinder, twelve sheets were extracted axially using WEDM. The last figure (in the range of 1...12) specifies the position of the sheet within the cylinder, i.e., where one and twelve are on the outside. The following letter (A) states the sheet orientation in the macroscopic specimen—technically this could be axial, radial, diagonal or similar—but here only "A" referring to axial was used. The last term (BR, MT, MS) indicates the test the sample is designated for and is dependent on the geometry. "BR",

[3] $f \propto \sqrt{k/m}$, k...stiffness of gage section, m...mass at the free end.

"MT", and "MS" refer to bending resonance fatigue test, microtensile test, and metallographic specimen, respectively. Rather than having, e.g., a sample "2" and a sample "11" without indication of geometry, location, or intended test, this repeatable system was designed to distinguish easily between samples without the need of a database or list, which is often not at hand in the laboratory. Additionally, the "mother" components are also labeled within this system. For example, the macroscopic fatigue specimen two is "2000" and cylinder one from macroscopic specimen two is "2100". The bending resonance fatigue specimens derived from this cylinder (its children) are therefore labeled "AZI-2101...2112-A-BR".

The first tests were performed with two samples polished in accordance with table 3.1, without the electropolishing step. These samples—AZI-2202-A-BR and AZI-2203-A-BR—were tested at 360 MPa stress amplitude for about 380,000 cycles and failed due to crack initiation at the original specimen edge. This area was known to concentrate stresses (as can be seen in fig. 3.3b, the highly stressed region extends onto the sidewall) and the surface roughness was much higher on the sidewalls, as they were still in the as-machined condition. Multiple cracks initiated at the top and bottom of the gauge and propagated inwards. The test, however, was not considered as a failure, and multiple conclusions could be drawn from this initial test:

- Rounding of the edges is absolutely necessary to avoid crack initiation at geometrical features and to provoke crack initiation at locations of increased stress due to crystallographic features as featured in Refs. [13, 18, 21, 30, 35, 38].
- Crack propagation was found to be similar as in Refs. [39, 40].
- Some cracks at the edge initiated under a 45-60 ° angle to the sample's "loading direction" near TBs. This was later established as the main source of cracks located in grains in the center of the samples. It appears that if the stress concentration from the sharp edge overlaps with a grain fulfilling the criteria for crack initiation (from section 2.3) it will also lead to crack initiation.
- The backscatter detector of the SEM was impressive at portraying the microstructure around the crack including γ' precipitates, TBs, GBs and the fine and localized slip bands near cracks with high plastic deformation. The BSD was hence selected as the main detector for images for crack analysis and DIC.
- EBSD analysis was very successful and the OPS-polished specimens showed a high image quality. This was one of the reasons for repeating OPS-polishing after electropolishing at a later time.

The third test was conducted on specimen AZI-1103-A-BR in order to determine the effectiveness of the electropolishing process in terms of surface smoothness and edge roundness. These features were checked with the optical and electron microscope and subsequently considered sufficient for bending resonance fatigue. The surface was also checked for EBSD patterns, but the image quality was found to be significantly worse than in specimens 2202 and 2203, which had been OPS-polished but not electropolished. Thus the aforementioned OPS-polishing was used for all samples after this (i.e. the samples in table 4.1). The specimen AZI-1103-A-BR was fatigued in the setup first at 100 MPa, because of the findings of Alam et al. [18] with a very similar setup. They reported microcracks after fatiguing for about 500,000 cycles at 80 MPa. Specimen 1103 however, showed no microcracks or slip markings in the SEM after approximately 100 million cycles. It was therefore tested again at 400 MPa. It failed within the first few hundred thousand cycles, showing type I cracks starting again under a 45-60 ° angle relative to the loading direction in the center of the bending beam. With increasing numbers of cycles, some cracks started to grow outwards and two of them reached the edge of the sample. A large amount of extruded material was found at the cracks and their cyclic evolution can be seen in fig. 3.4.

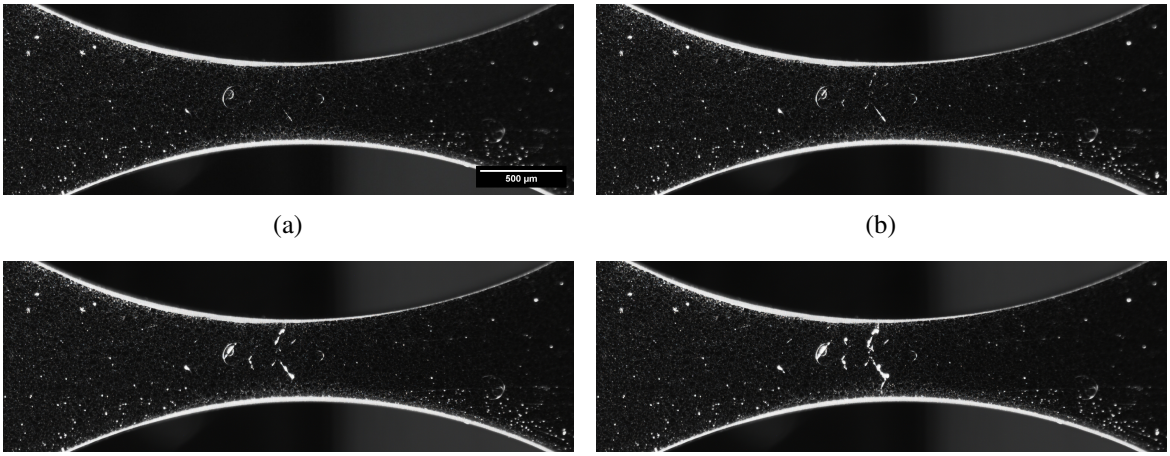

(a) (b)

(c) (d)

Fig. 3.4 In-situ darkfield images from the bending resonance fatigue test of sample AZI-1103-A-BR at 400 MPa showing the marked surface. Between the first subfigure a) and the last subfigure d) 226,807 cycles were applied. The mass is located on the right-hand side.

After this third preliminary test, the testing parameters were fully defined for the main tests; a total of four specimens were prepared by grinding and polishing followed by electropolishing and another OPS-polishing step. Subsequently, the samples were subjected to BSD scans of both sides before and after testing, EBSD scans before testing, and bending resonance testing with fully reversed stress amplitudes of around 400 MPa (see also fig. 3.1).

Chapter 4

Results

4.1 Specimen AZI-1104-A-BR

Samples AZI-1101-A-BR, AZI-1104-A-BR, AZI-1105-A-BR, and AZI-1106-A-BR were selected due to their ideal thickness between 225 and 240 µm. The preparation was the same for all four samples and there were no major differences in surface quality (i.e. image quality and confidence index, see section 3.2) amongst them. Since sample AZI-1103-A-BR failed at 400 MPa, it was expected that the same would be true for these next samples; AZI-1104-A-BR was the first to be tested and it was decided to first go with a lower stress amplitude and enter the VHCF regime. A stress amplitude of 300 MPa (corresponding to 1.02 V) was chosen for the first test with the goal to generate slip markings and microcracks for a cycle number greater than 10^7 as in Refs. [18, 30]. After about 75 million cycles, the test was stopped, as neither a decrease of the resonance frequency nor damage on the sample surface was observed. The voltage was linearly increased to 1.1919 V ($\widehat{=}$ 350 MPa). After one hour and approximately 6 million cycles, again no sign of fatigue was observed. The voltage was once more increased to 1.36 V ($\widehat{=}$ 400 MPa) and the specimen was fatigued for another 8 million cycles. At this stress amplitude, the f_{res} increased slightly—a sign of work hardening. At 400 MPa, sample AZI-1103-A-BR had previously failed quickly, but not this specimen. It is assumed that this is related to the thickness—1103 was significantly thinner than 1104 (below 200 µm) and hence a much higher voltage (and deflection) was necessary. It was then decided to try 450 MPa and to initiate microcracks.

Indeed after a few hundred thousand cycles, one small crack was visible in the darkfield image and the test was stopped. The subsequent investigation in the SEM revealed one crack (type III) on the marked surface[1] and four more on the opposite side (see fig. 4.1). However,

[1] Marked side refers to the surface visible in the darkfield camera.

of the total of five cracks on both surfaces, one crack initiated at the edge (i.e. the crack which was seen in the live darkfield image on the marked side and not the cracks annotated with arrows in fig. 4.1), and two others started at pores and were determined as not relevant to this study. Since the grain at the edge, in which a crack initiated, was also oriented for high shear and the crack began along a TB, it could be that this grain fulfills the criteria for crack initiation and either the (rounded) edge had no influence on the crack initiation or some stress concentration was still present and caused the crack. Edge initiation was also observed for other specimens but not more than five times.

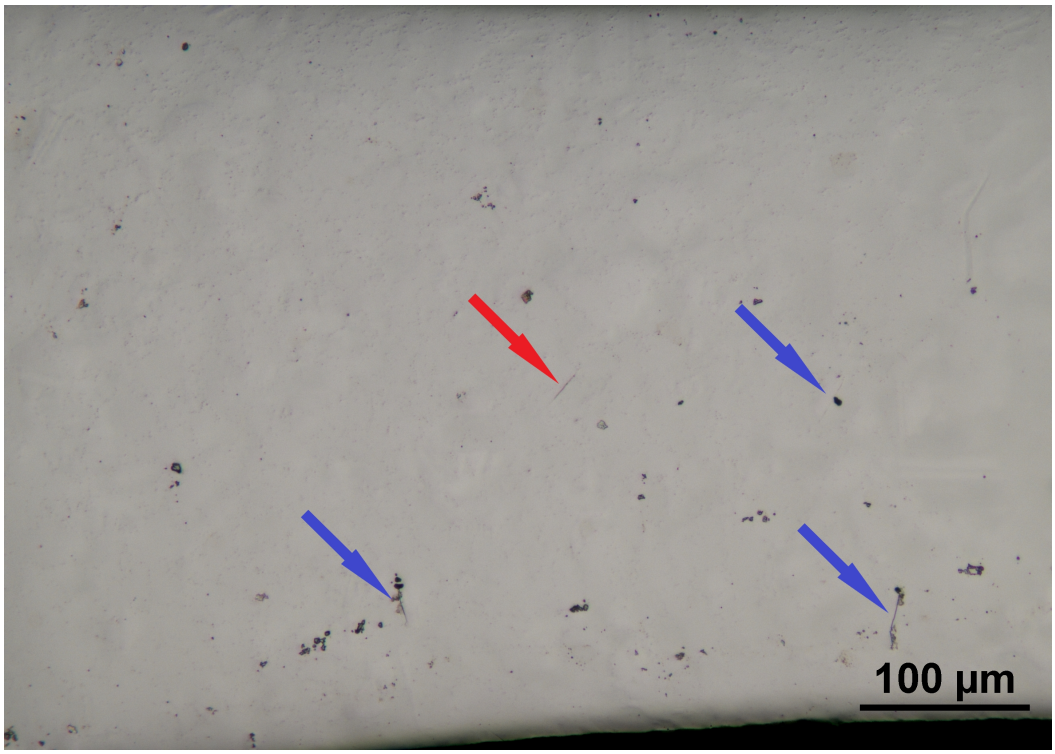

Fig. 4.1 All four cracks on the non-marked side of specimen AZI-1104-A-BR as seen in the light microscope after 267,340 cycles at 450 MPa. Blue arrows indicate cracks in the vicinity of a pore, red arrows indicate regular cracks.

After this test at 450 MPa, it appeared as if a suitable stress level had been found to fatigue the nickel-based superalloy Rene'88DT in the LLF/HCF regime. Therefore the next specimen was also tested at 450 and the last two at 425 MPa, to have some variance in stress amplitude. Testing in the VHCF/UHCF regime was dismissed because neither cracks nor slip markings had been observed to initiate, at least not for the applied number of cycles and the given stress amplitude. This absence is discussed in section 6.2.

4.2 Specimen AZI-1105-A-BR

The next sample was not used to find a decent stress level but was directly fatigued at 450 MPa ($\widehat{=}$ 1.53 V). AZI-1105-A-BR was of similar thickness as AZI-1104-A-BR and had a higher resonance frequency. The specimen was fatigued again until small cracks were visible in the darkfield image. The test was stopped there to prevent further propagation of cracks and to be able to analyze the grain in which the microcrack had initiated. Approximately 610,000 cycles at the desired stress ($\pm 5\,\%$) had been applied until this point. The evaluation of the number of cycles was done after the test with a specifically designed Jupyter notebook and the metadata from the test setup. Overall, eleven cracks were counted on the marked side in the SEM, one initiated at the edge and one at a pore. The non-marked side showed only four cracks, which were all associated with features in the microstructure rather than pores or the specimen edge.

4.3 Specimen AZI-1106-A-BR

After two successful tests at 450 MPa it was decided to lower the stress to 425 MPa and have two more tests with a higher number of cycles. The first specimen at 425 MPa was AZI-1106-A-BR with a thickness of about 240 µm and a f_{res} of 1510 Hz. The voltage for this test was 1.434 V, because the sample was thicker than the previous two. During the gradual increase of the voltage, the phase angle had problems catching up and plateaued multiple times before reaching the target stress. This might have been caused by problems with the clamping. However, once the sample had reached the stress of 425 MPa, cracks were visible shortly after and the test was stopped. The number of applied cycles was only about 30,000—significantly fewer than for the other samples—probably due to one of several affecting issues. One of such may have been the larger-than-average scratches on the marked surface of AZI-1106-A-BR. Maybe the test was stopped sooner than for other specimens because AZI-1106-A-BR showed no type IV cracks and only three type III cracks. Nevertheless, the crack distribution, initiation, and propagation is identical to other specimens and therefore the test was considered valid.

4.4 Specimen AZI-1101-A-BR

The last specimen was AZI-1101-A-BR with a thickness of about 240 µm and a resonance frequency of 1344 Hz. The stress was 425 MPa ($\widehat{=}$ 1.434 V) and the goal was again a cycle number higher than in specimens 1104 and 1105 while maintaining microcrack initiation in

the sample and avoiding fatal cracks. The progression of the test is depicted in fig. 4.2. The starting point is after the frequency sweep at about 400,000 cycles. The stress during the sweep was below 100 MPa and therefore not considered as relevant for the evaluation. Then the stress amplitude increases quickly, this is where the voltage was increased step-by-step to let the phase angle catch up after each increase. When it reaches the target stress (cyan horizontal line) it does neither increase nor decrease for the duration of the test (about twelve minutes). This once again shows the true meaning of "damage tolerant", because four type I, two type II, and one type IV cracks had already formed on the two surfaces of the specimen. The frequency sweep after the test showed that the f_{res} decreased by about 3.6 Hz, a sign of fatigue damage, but it still remained intact and could withstand the stress.

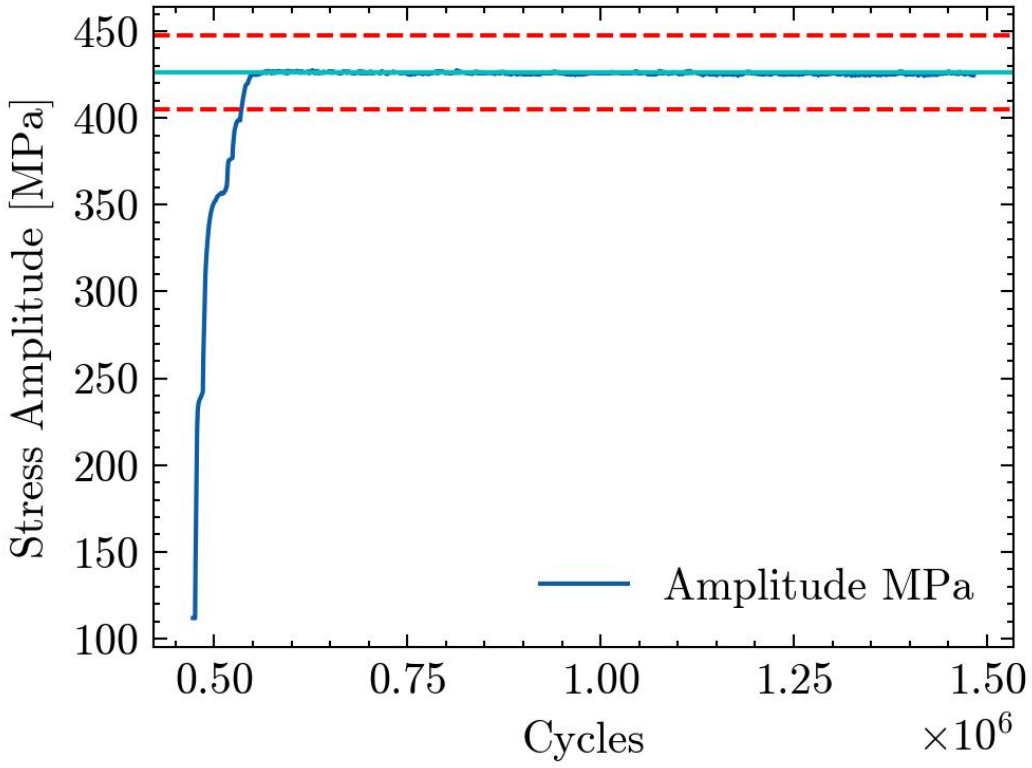

Fig. 4.2 Von Mises stress amplitude over cycles for the sample AZI-1101-A-BR. The target stress of 425 MPa is shown in cyan and no deviation during the fatigue test can be observed. Within the dashed red lines—the ±5% range—950,000 cycles were recorded.

4.5 Overview of fatigue results

Table 4.1 Overview of the bending resonance fatigue of the final four samples with the number of cracks for each specimen, including the ones initiating at an edge or a pore.

ID	σ [MPa]	f_{res} [Hz]	Δf_{res} [Hz]	Cycles at $\pm 5\%\sigma$	cracks
AZI-1101-A-BR	425	1343.7	-2.6	948,736	7
AZI-1104-A-BR	300	1333.9	-0.9	74,592,052	0
AZI-1104-A-BR	350	1333.0	-0.5	5,977,338	0
AZI-1104-A-BR	400	1332.5	+1.0	8,071,645	0
AZI-1104-A-BR	450	1333.5	+2.4	267,340	5
AZI-1105-A-BR	450	1469.5	-4.7	608,518	14
AZI-1106-A-BR	425	1513.0	-1.1	30,585	31

To sum up, four bending resonance fatigue specimens were tested at their resonance frequency in a unique setup that allows visual as well as mechanical damage observation (e.g., a change of the resonance frequency). This combination allows the researcher to stop the test, once a certain criterion is reached. In this case, it was the initiation of microcracks (type I) on the polished surface. The goal of this work was not the generation of a Wöhler curve, a double-logarithmic stress amplitude over cycles diagram, where specimens are being tested at different loads until their failure.[2] Instead, the location for crack initiation and the early stages of crack propagation with respect to microstructural features were of interest. Therefore, the cycle numbers of the tests in table 4.1 cannot be seen as cycles until failure, but rather as cycles until the defined criterion was reached. Specimen AZI-1106-A-BR should be considered as a special case because the gradual increase of the voltage (i.e. the stress amplitude) was not as smooth as for the other specimens, with potential reasons discussed in section 4.3. Nevertheless, all tests were considered successful, as a total of 57 cracks could be created and their initiation point could be determined with respect to the microstructure. Twelve of them initiated in the vicinity of a pore or started at the edge and were therefore not considered as relevant for the investigation. It however reaffirms, that microstructural defects such as pores and geometrical defects like edges and notches have a negative influence on fatigue life and favor crack initiation and ought to be avoided. This does not mean that for all these cracks the pore or edge was the only reason for crack initiation, but it cannot be disproven at this point. The 45 cracks initiating in the specimen interior were then divided into four types of short surface cracks (see fig. 4.3), following the nomenclature of Bataille and Magnin from Ref. [29]. Type I cracks are constrained to one grain and are hence often

[2] The failure can either be defined by a certain drop in force or a complete breaking apart of the specimen.

referred to as microcracks. Type II cracks propagated across two or three grain boundaries and are still not larger than three times the average grain size. Type III cracks are longer than three but smaller than ten grains and type IV cracks are longer than ten grains. Bataille and Magnin claim that typically a sample cannot contain more than one to three type IV cracks and that they form (out of a type III crack) in the last 10% of the lifetime [29]. Stinville et al. [41] claim that the type IV cracks were observed after 80% of lifetime in their axial fully-reversed fatigue of Rene'88DT of cylindrical specimens. In this thesis, the samples were not fatigued until end of lifetime, but the classifications from Bataille and Stinville still gives a good indication, if the specimens were close to failure or not.

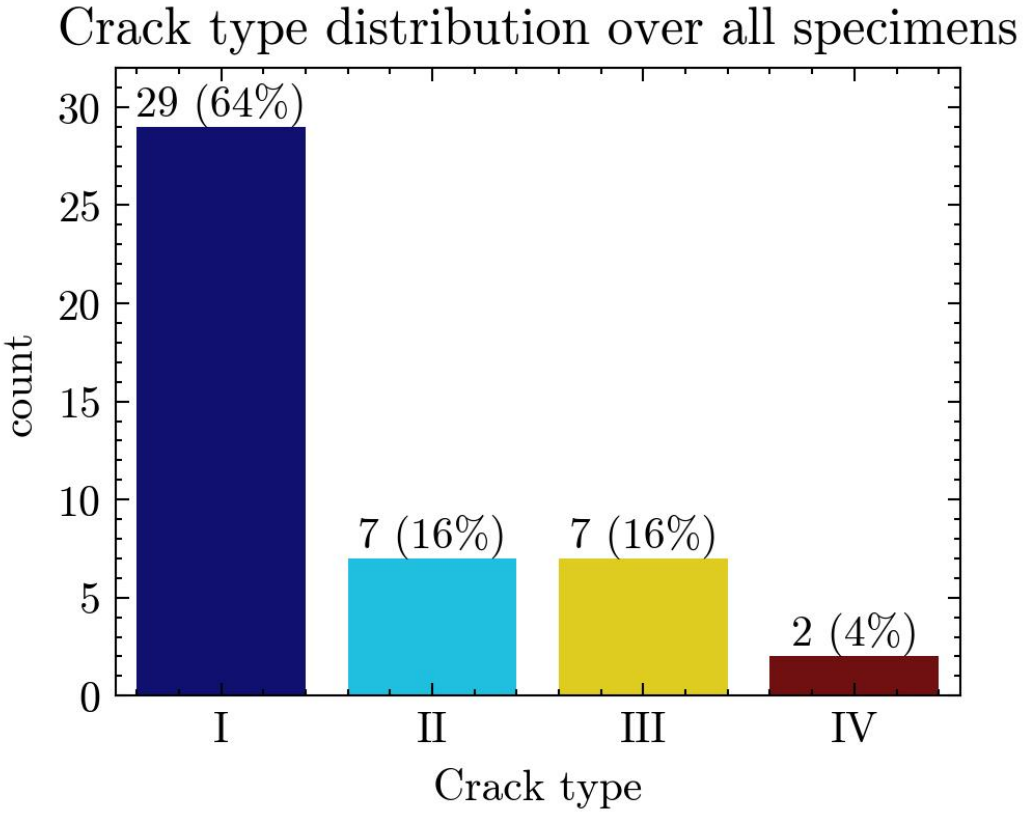

Fig. 4.3 Crack type distribution following Bataille and Magnin [29] (in absolute and relative numbers) of cracks for all four specimens, excluding cracks at pores and edges.

4.6 Crack types and their numerical distribution

Type I cracks: 29 microcracks were recorded, 22 of them solely on specimen AZI-1106-A-BR. All of them were found to initiate close to TBs.[3] In the aforementioned sample, three categories could be established corresponding to the 2D morphology of the twin in the parent grain.[4] Lenthe et al. [22] distinguish between four different morphologies; complete, incomplete, corner, and island. In this material, no difference was observed for complete and corner twins and so they were put into one category.
Complete twins: Twelve out of the 22 type I cracks were stopped at GBs on both sides of the grain. An example of this TB localization can be seen with crack I-9 in fig. 6.5.
Incomplete twins: Eight type I cracks were stopped at a GB on one side of the grain and ended inside the grain at the opposite crack tip (see fig. 6.5). Crack I-14 of about 10 microns length does not deviate from the twin boundary and ends within the grain, instead of continuing to grow and fig. 6.2 also shows an incomplete twin.
Island twins: Two cracks did not even reach a GB on either side and ended within the grain.

Type II cracks: In total, seven cracks that spanned across two or three grains were counted. This number is significantly lower than the number of type I cracks and indicates that many microcracks did not propagate further. However, six additional type II cracks were not considered in this evaluation because of their vicinity to an edge of the specimen or a pore (cluster).

Type III cracks: A total of seven type III cracks were counted on all four specimens and their growth deviates from shorter cracks, as they do not necessarily propagate along TBs after leaving the initiation TB but intragranularily along the activated slip planes of neighboring grains. Type I and II cracks were found to propagate very straight, but type III cracks did not show such morphology and most of the time a zigzag-like crack pattern was observed, similar to [40]. A common observation was also a cracking across multiple parallel planes and sometimes a rejoining further down the grain, where the piece inside (of somewhat rectangular shape) would break out or protrude.

Type IV cracks: These cracks extend over at least ten grains and were rarely observed in our tests, but this can be accounted for by the criteria that were set to end a test. If a routine with interrupted tests had been chosen, the specimens could have been fatigued until final fracture (load falls below a certain level or crack extends across the whole sample) and more type IV cracks would have been observed. The two type IV cracks recognized in this study propagated along the activated slip plane as can be seen for crack B-03-IV from specimen

[3] This offset was not quantified in this investigation, however, Stinville et al. claim it is around 0.8 µm [20].
[4] The same behavior was observed in the other samples too, but here it is illustrated only for one due to the higher type I crack density.

AZI-1101-A-BR (marked side) in fig. 6.4. They also show a great number of branching incidences and the zigzag crack path of type III cracks can be observed here as well.

Chapter 5

Computational analysis of specimen microstructure

Microstructure analysis was mostly done with the Matlab free and open-source toolbox MTEX, as it offers a comprehensive selection of evaluation tools and a high degree of customization. Some process accompanying assessments were done in the proprietary EDAX OIM software. In OIM it is fast and user-friendly to do an analysis and it can be utilized to check data quickly after an EBSD scan. It does, however, not offer the multitude of functionalities and customizations that MTEX allows for. With these EBSD data analysis tools, the orientation of the grains could be visualized (i.e. an IPF map) and subsequently numerous evaluations were performed, e.g., Schmid factor, slip systems, and Burgers vector analyses.

The Ni_3Al precipitates were clearly visible in the HDBSD images and allowed to assess local displacements based on digital image correlation on the HDBSD images, due to their high contrast, their regular distribution, and random spacing. The deposition of gold particles, as it is often used for small-scale DIC investigations, was not necessary [42]. The gold particles would further interfere with the EBSD and the use of HDBSD images presents an easier and more flexible alternative. The ex-situ HR-DIC was used to visualize the plastic deformation that had occurred in the vicinity of short and long cracks. The usage of the inherent precipitates also allowed to depict the shearing accurately, because the particles, due to their small lattice mismatch, may be cut by dislocations during plastic deformation. The entire workflow of this DIC process is described in section 5.2 and comparisons with former similar investigations are drawn in the discussion section of this thesis (in chapter 6).

5.1 Microstructure analysis with MTEX

MTEX is a free and open-source toolbox for the commercial software Matlab (from *MAT*rix *LAB*oratory) developed by geologists, EBSD experts, and data analysts to assess a multitude of crystal properties. Many of the analysis tools used by researchers are not free, and sometimes not even generally accessible. The focus was therefore on the analysis methods of section 2.3.1, their replication in MTEX and to assess the differences and similarities of the results.

First of all the relevant data had to be recorded. The specimens were scanned before testing in the SEM using the EDAX Velocity camera series and the EDAX APEX software. A sample tilt of 70 degrees was necessary and the step size within a rectangular grid was set to 0.5 µm to resolve also thin twins which are present in the material. The data was then exported as a *.ang file (i.e. a file containing metadata and binary data of every point of the EBSD measurement) with the relevant information including the three Euler angles in radians, the relative x- and y-coordinates in microns, the image quality (IQ) and the confidence index (CI) dimensionless. The *image quality* is similar to Oxford Instrument's *band contrast*, a measure of how sharp the Kikuchi patterns appear in terms of contrast. This gives an indication of how free of deformation the sample surface is and consequently, how well specimen preparation was done. Scratches, particles on the surface, or grain boundaries have a smaller IQ [43]. The CI measures the reliability of pattern indexing and ranges between 0 and 1. The CI was generally quite high among the specimens in this thesis because nickel is a well-suited material for EBSD. Using MTEX's import wizard the data was then loaded into Matlab. The import wizard helps transfer the data into the designated variables, arrays, and matrices. First of all the crystal symmetry needs to be defined by the three crystal lattice constants a, b, and c, which are equal for a cubic system.[1] The crystal point group was taken from the *.ang file as 432 and the only indexed phase was nickel. The Euler angles were then converted into spatial reference frames with setting 2, which is standard for EDAX *.ang files, and made up the EBSD variable. The inverse pole figure (IPF) color key (fig. 5.2) was assigned and the direction for the IPF was set parallel to the z-axis, hence coming out of plane. The grains were constructed with a minimum size of eight pixels and a minimum misorientation of two degrees. A grain smoothing with factor 5 was applied, interpolating the grain boundaries to get rid of the rectangular, step-like shape from the acquisition. This smoothing does not affect the grain boundary misorientation. With the "inpolygon" command, a certain ROI of the EBSD scan could be selected and reduced calculation time for future processing.

In fig. 5.1 the four relevant MTEX analyses are depicted at the location of a type II crack.

[1] 3.59 Å was chosen for a, taken from Ref. [7].

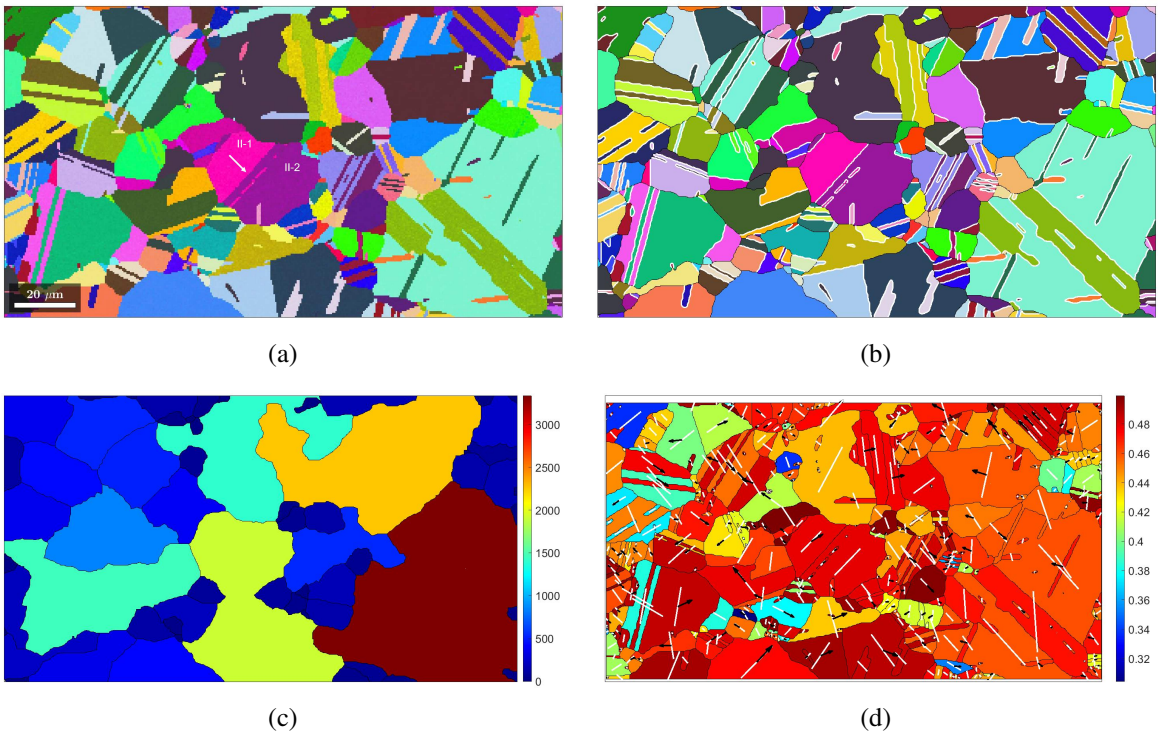

Fig. 5.1 Overview of the type II crack location used for HRDIC in section 5.2 and HDIC in section 5.2.4 and surrounding areas with different material characteristics. The micron bar applies to all images; a) IPF map. The crack initiated in grain II-1 at the tip of the arrow, parallel to the TB. The corresponding IPF color key can be found below; b) IPF map with twin boundaries indicated in white; c) Map of merged grains that share a LAGB with 20 ° misorientation or less. The color of the grains is according to their size in μm^2; d) Schmid factor map (unitless) with activated slip planes (white) and Burgers vectors (black arrows).

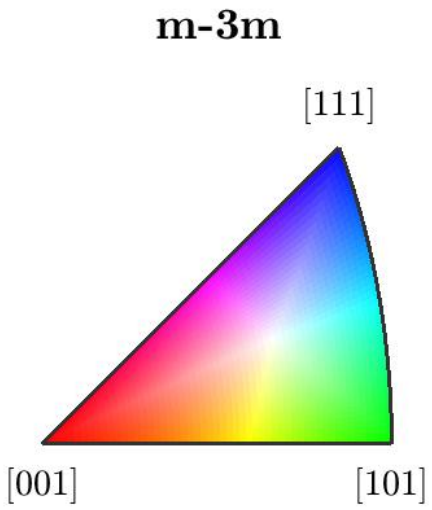

Fig. 5.2 IPF color key for Rene'88DT

5.1.1 Schmid factor calculation and active slip systems

The Schmid factor (see section 2.2.2 for calculation and history) is a measure of resolved shear stress and is a function of the crystal lattice rotation in the specimen for a given stress tensor. Hence, in a polycrystalline material, the SF will differ from grain to grain. The calculation and plotting thereof was done with the following steps in MTEX.

First of all the slip systems of the FCC lattice are assigned to the slip systems variable and a symmetry operation is applied to obtain the possible permutations for all twelve slip systems as combinations of $\{1\,1\,1\}$ planes and $\langle 1\,1\,0\rangle$ directions. Next, the slip systems have to be rotated from crystal coordinates into specimen coordinates. The stress tensor is defined as uniaxial along the x-direction—the longitudinal direction of the specimen. Even though the loading is in fully reversed bending, the von Mises stress on the sample's surface is mainly uniaxial, as was confirmed with the FE analysis. The SF can then be calculated as described in section 2.2.2 with the two relevant angles. Only the maximum SF is relevant and therefore the activated slip plane is selected and rotated into specimen coordinates. Lastly, the grains are plotted and colorized with their corresponding SF (colormap *jet*), the trace of the active slip system is plotted for each grain in white and the Burgers vector in black as can be seen in fig. 5.1d, fig. 6.4 and fig. A.4. If the Burgers vector is not visible, it points perpendicular either out of the surface or into the surface.

5.1.2 Twin boundary analysis

Twin boundaries play an important role in fatigue crack initiation and local strain accumulation. Their multitude and magnitude can be of importance and were therefore analyzed as well. This step was also necessary to exclude TBs from the grains for evaluations described in section 5.1.3.

Starting with the EBSD variable, the grain boundaries are saved to a separate variable and in the next step, all nickel-nickel GBs within the frame are selected and all edges of the scanning frame, that the software would also see as a grain boundary, are excluded. This GB variable has three properties; misorientation, segment length, and direction. Obviously, to distinguish between a regular GB and a TB the misorientation is the important property. After saving the angle of all GB misorientations to a variable and transforming it from radians to degrees, a criterion can be set that the angle for a TB shall be smaller than 61° and greater than 59 °. When these misorientations are scattered in an axis angle domain, a clustering can be observed and a twinning relationship established:

```
mori = GB_NiNi.misorientation(GB_NiNi.misorientation.angle ...
>59*degree & GB_NiNi.misorientation.angle<61*degree);
```

```
scatter(mori)
mori_mean = mean(mori,'robust')
round2Miller(mori_mean)
```

This twinning relationship comes out to a special combination of plane and direction, which defines the twinning as a rotation of 60.000° about the $(1\,1\,1)$ axis. With this, each grain boundary segment can be analyzed if it fulfills the twinning criterion and can subsequently be plotted in a different color than the GB (see fig. 5.1b).

5.1.3 Calculation of grain boundary misorientation and its modification

The `TB` variable, which contains all twinning elements of the GB variable, can now be used to merge parent and twin grains. Because the aim was to plot grain clusters of misorientation up to 20 °, an extended `merge` command was used for a certain threshold of misorientation angle:

```
[grainsMergedCombined] = merge(grains,TB,'threshold',20*degree);
```

The result is a grain map with the same features as by Miao et al. [30], where grains separated by LAGBs are merged because it was claimed that cracks would favorably grow in such grain clusters excluding TBs. Rather than random RGB colors for the grains, the color code was selected as a function of grain cluster area size to enable a better visualization (see fig. 5.1c).

5.2 High-resolution digital image correlation in Python

Ex-situ HRDIC refers to a sub-grain resolution of plastic strain for experiments that are not continuously imaged and correlated but are interrupted during or even finish the experiment before taking additional micrographs. The DIC captures fine details in the grey scale of the image pixels and is not dependent on any length scale. This means, the finer the details within the correlated image, the higher the resolution of strain [44]. In standard DIC tests, this would refer to the speckle distribution and size—limited by the particle size. In this setup the fine γ' precipitates appear darker than the matrix in the HDBSD micrograph, allowing for an extremely fine pattern due to their size of 150 nm on average. However, the imaging in the SEM is also associated with some difficulties for HRDIC: (i) introduction of drift and noise (ii) spatial distortion similar as in optical lenses, especially pronounced for lower magnifications, and (iii) uncertainties in SEM magnification due to deviations in magnification in the order of 3% [44].

In this thesis, (i) and (iii) were (partly) corrected with the instructions from Mello et al. [44]. To reduce spatial distortion, a micro-pattern would have been necessary on the specimens, and an elaborate computational transformation, which would have exceeded the scope of this thesis.

5.2.1 SEM corrections

The charge-induced, the material stress relaxation and the thermal drift as well as the image noise were minimized by working at a lower acceleration voltage of 10 kV rather than the 20 kV from EBSD, selecting an aperture size as large as possible (i.e. 60 µm), decreasing the working distance, and increasing pixel acquisition dwell time. For every scan, the histogram was optimized to have a good grey scale distribution. The probe current, spot size, and grounding (increasing contact area and conductivity) could not be altered in the Sigma 300 SEM and were standard settings.

The magnification deviations were dealt with as suggested in the paper, starting from a high magnification and decreasing it until the desired value was reached. Additionally, scans for DIC were taken at the same magnification.

One initial idea was to select areas in the specimen and scan them separately from the large area scan at a higher magnification of $5,000\times$. This would reduce distortion and focus issues, but unfortunately only one of the selected areas developed a microcrack during testing. This crack was less than 10 µm long and the local plastic deformation was not sufficient to be evaluated. Therefore, specific regions (ROIs) of the large area scans where cracks initiated were selected. This ensures higher plastic strains that can be optimally analyzed and reduces time.

5.2.2 Image registration

The images were cropped from the stitched large area scans using a simple Python script with Python imaging library (PIL). In order to overlay the second image taken after the test ("post") onto the initial one taken before the test ("pre"), homologous points on the right side of the images were selected, as this side was the clamped side at which the damage-induced image differences should be comparatively less. The high contrast in the images was extremely useful as it allowed for a very accurate point selection. When zoomed in, the precipitates appeared as dark spots of only a few pixels, and one could select the same precipitate in the pre and post image. For each image, a minimum of twelve points was selected and distributed along the entire height with a small horizontal offset. The coordinates of the selected points were saved for the next step.

These points from the selection GUI were then transferred into the registration python file using the SimpleITK image analysis toolkit to register the image and to estimate the transformation to the pre image coordinate system. An affine transformation was selected to resample the post image. The affine transformation uses a linear transformation plus a constant offset to transfer coordinates. This geometric transformation with six degrees of freedom preserves parallelism and lines but not necessarily angles and Euclidian distances. This type of transformation was selected because the misalignment of the images needed to be eliminated, while local non-linear discontinuities (cracks, PSBs) needed to remain unchanged to evaluate them with the DIC. An affine transformation, for example, from the coordinate system 1 into the coordinate system 2 could look like this for an n-dimensional vector x_1:
$x_2 = A * x_1 + b$, where A is a constant $n \times n$ matrix and b is the constant offset [45].

5.2.3 µDIC toolkit

The µDIC toolkit was developed at the Norwegian University of Science and Technology in Trondheim and the SINTEF Department of Materials and Nanotechnology, is a toolkit for digital image correlation analysis in Python. The package utilizes B-spline elements to discretize the deformation field. With this FE-based DIC, the inter-nodal coordinates are interpolated and a high order continuity is ensured by using the aforementioned B-splines. This is different from subset DIC (see Open-DIC, section 2.3.1), where independent subsets are correlated. The correlation is done with a Newton-Raphson scheme to minimize the sum of squared differences in the grey scale values of the pre and post image. The exact analytical formulations and algorithms can be found in Ref. [46]. In this module the user can choose the number of images, the number of points for the finite element discretization and their spacing, as well as evaluated variables such as displacement, true strain, or engineering strain. The module is free and open-source but requires some other packages such as numpy, matplotlib, and skimage.

After the resampling of the deformed image in the last subsection, the pre and post images are then cropped to the same size and loaded into the µDIC toolkit as an image stack. A GUI pops up where the ROI can be selected and meshed. The mesh can be adjusted in terms of the number of knot vectors in x- and y-direction, which also shows the spacing between the points in pixels. If the distance between the points was chosen too small, artifacts were recorded. During the thesis, it became evident that the sweet spot lies between 60 and 100 pixels. Following the meshing, the DIC software will evaluate the data using a non-linear least squares solver for image correlation. The output can be displayed as displacement or

strain and a modification to the code was made during this thesis to evaluate different features one after the other, without having to redo the mesh generation step.

The first evaluation was a type II crack from specimen AZI-1104-A-BR on the non-marked side (the location of the crack is at the tip of the white arrow in fig. 5.1a). This crack initiated at a Σ3 TB and propagated a short distance into two neighboring grains. The pre and post image were processed as stated above and evaluated for true strain and displacement in x- and y-direction.[2] The discrete points (i.e. the knot vectors of the mesh) were selected with a number of 32 in x-direction and 26 in y-direction for the ROI which translated to a spacing of 66 pixels. To display the results, a quiver plot of displacement was chosen because it facilitates presentation compared to a contour plot. In the quiver plot, each arrow represents a point that was chosen in the GUI as an element. Its length is scaled for visibility and does not display the real displacement length.

The results clearly show a displacement of the grain along the crack. The left side is displaced from the right side, because of the crack opening. Generally, displacements in y-direction are evident, especially to the left of the crack.

To ensure the software is working properly, the exact same images were analyzed using the software GOM correlate 2016. Instead of a full set of points like in the μDIC, singular "facet points" were selected and distributed randomly across the grain with the crack and some neighboring grains. The evaluation was set to analyze the displacement in x- and y-direction. The result was a displacement vector for each point, consisting of a value dx and dy, scaled to the screen size. The displacement vectors qualitatively validated the quiver plot of the μDIC. The furthest left point showed the greatest negative x-displacement and the greatest positive y-displacement. The furthest right point had a very small displacement in positive x- and negative y-direction. Points on the right side but next to the crack showed a positive x- and y-offset, significantly greater than the point furthest right. Points on the left side, close to the crack showed a smaller negative x-displacement but a two- to five-fold increase in positive y-displacement than the points near the right crack edge. Overall, it can be said that the left side of the grain was displaced to the left and up and the right side only slightly up and right, or not at all, as was evaluated with both of the two independent softwares. Further details are discussed in section 6.3 comparing the results with Heaviside DIC.

Another evaluation was done on the type IV crack from specimen AZI-1101-A-BR marked side (fig. 6.4). This crack has been discussed previously in section 4.6. The location of the initiation (grains IV-1 to 4) was not evaluated because the great amounts of extruded material made DIC impossible there (i.e. the underlying displacement was hidden). Instead,

[2] x refers to the longitudinal direction of the sample and y to the width of the sample.

the propagated crack was investigated in a neighboring grain. This grain contained a rather large twin, spanning across the whole grain and being oriented parallel to the activated slip plane. This region was correlated with a point set spaced 72 pixels in x- and y-direction. The displacement plot showed no notable displacements along the crack. Note that this is not a crack initiation location but rather a propagation site in a favorably oriented neighboring grain. However, it revealed an unexpectedly large displacement in y-direction in the twin next to the crack (about 500 pixels to the right). This displacement was visible on both sides of the twin and quantified with about 8 pixels, which equals to about 0.15 µm.

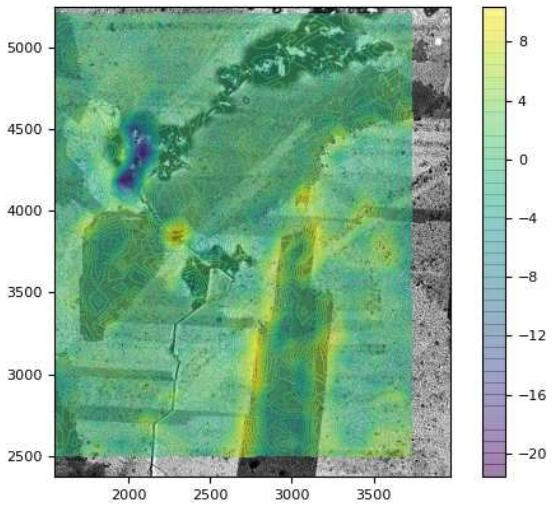

Fig. 5.3 Displacement map in y-direction of the bottom part of the type IV crack (see also fig. 6.4) with the displacement in pixels showing a local concentration at the TB right of the crack. The HDIC also showed high plastic deformations for this section of the crack (described in section 5.2.4).

5.2.4 Heaviside DIC

HDBSD scans from this thesis have been sent to Jean-Charles Stinville and Rephayah Black from the University of Illinois Urbana-Champaign to evaluate them with Heaviside DIC (HDIC). This discontinuity-tolerant HDIC utilizes the Heaviside function to measure quantitatively plastic localizations in the material even if discontinuous kinematic fields are present due to the emerging slip bands. Discontinuities can be analyzed for their inclination, position, and slip system. The strain around a crack or slip band can be calculated and displayed [47]. The achieved resolution is stated with four to ten nanometers and results can be evaluated with Python or with maps as in fig. 5.4. The images were analyzed for the norm

of the in-plane slip vector $||\vec{\tau}||$, the angle of the in-plane slip vector γ and the strain ε_{xx}. The results from the slip vector are in pixels and have to be multiplied by the factor of the image acquisition of the SEM (see table A.1). The angle is calculated in radians and needs to be transformed into degrees and states if the displacement at a slip band/crack is purely in-plane shearing (0 °/±180 °), purely in-plane sliding (± 90 °), or mixed.

The images in fig. 5.4 are displayed using a look-up table (LUT) from ImageJ free software. Note that the noise in the data for the angle is larger; this is a consequence of the analysis algorithm and because angular displacement is independent of the length of the displacement vector. The two positions of section 5.2.3 were evaluated with the HDIC. The displacement angle γ at the initiation site of the type II crack is between approximately 68 ° and 105 °. Slip is therefore more sliding than shearing and oriented towards the top left of the image. The displacement vector length at the crack shows higher values in the middle of the grain and decreases towards the respective grain boundaries and beyond. The maximum displacement (in x- and y-direction) was quantified with 92 nm. The plastic strain at the crack is in the range of ± 0.4 % but evenly positive, except for a few parallel areas where compressive strains can be observed, similar to results in Ref. [41].

The type IV crack evaluation was only performed for a ROI containing the crack propagation through a favorably oriented grain, not parallel and close to a TB (same as in section 5.2.3). Along the crack path, parallel bands rotated approx. 45-60 ° to the crack direction can be observed in fig. 5.3 toward the bottom of the picture. These bands were considered as “slip bands on a slip system that is not the one with the highest Schmid factor” by Jean-Charles Stinville during an online meeting. We can see from the SF of the activated slip system for this grain (fig. 6.4) that the crack follows it precisely and that a slip system with a smaller SF may indeed be crossing it there. The high strains of up to 1 % could be an influence as to why the slip bands—which are believed to not be persistent slip bands—were observed to be activated here but not for the type II crack. These slip bands were similar to the ones depicted in fig. 6.3.

The length of the in-plane slip vector is between 150 µm towards the top of the frame and 84 µm at the bottom. A gradual decrease can be seen. The angle of the displacement is on average between 75 ° and 108 °, except for a few areas near the top, where γ is approx. 140 °.

The crack propagation part from the type IV crack appears to contain a higher degree of localized deformation because not only the norm of the slip vector is significantly larger, but also the plastic strain has increased tremendously. This indicates that the local plastic strain during crack initiation is not as high as compared to crack propagation.

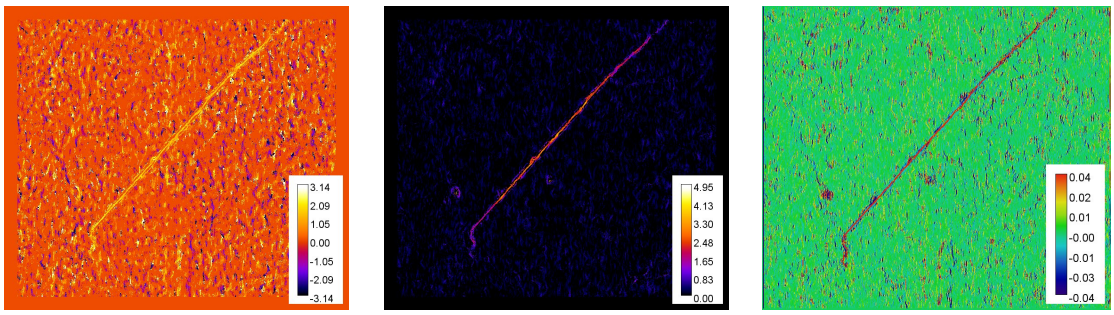

(a) (b) (c)

Fig. 5.4 a) Evaluation of the displacement angle γ in radians; b) Vector displacement length at the crack. The values can per definitionem only be positive and are shown in pixels. The maximum of 4.95 px corresponds to about 92 nm; c) Plastic strain ε_{xx} in percent.

Chapter 6

Discussion

6.1 Influence of detector selection for resolution of microcracks

In the experimental part of this thesis—contrary to previous investigations by Stinville et al. and Alam et al. [13, 18]—no extrusions and intrusions as the consequence of persistent slip bands and emerging before a microcrack as shown by Mughrabi [15] were observed on the surface of the superalloy following the cyclic fatigue testing. Although not proven, theories regarding this absence have been established during the course of this thesis. One involves the depth resolution of the backscattered electrons detector (see section 3.2). The BSD provides superior resolution of microcracks over the secondary electron detector, due to the nature of backscattered electrons. These electrons are primary electrons that are scattered within the material. Compared to secondary electrons they penetrate deeper into the material and may pass through thin sections like extruded material unscattered. The shear lips at extrusions are assumed to be such thin sections where secondary electrons are created but no scattering occurs. In the SE2 detector, extruded material was found to cover a crack or parts of it (see fig. 6.1a). A location like this might then be considered a persistent slip band with an extrusion or might not be recognized at all. However, with the BSD, the shear lip/extruded material appears to be too thin to scatter electrons, and subsequently, the generated image does not resolve the protrusion—it is transparent. The underlying crack, even if the lateral width is in the range of a few nanometers, is visible as a dark line in the BSD image. One instance where a crack was not visible with the SE2 detector but the detection was possible with the BSD is depicted in fig. 6.2. Extruded material covering the crack can be seen in fig. 3.2 in the lower part of the crack and in fig. A.2. However, it is not quite clear if these forms of material are shear lips or extrusions due to dislocation movement, or if the material

is emitted due to friction on the inside of the crack. It is, at this point, more likely to assume that the material is the result of a crack and not vice versa (see also section 6.2.2).

Alam et al. [18] describe the observation of multiple parallel slip bands in the EBSD image following the bending resonance fatigue test. Therein the alleged slip bands are pictured as dark lines. Unlike the sharp edges and clear contrast, they appear blunt and difficult to distinguish. Their trace across a TB seems more like a shadow in the EBSD. Furthermore, it seems that in the micrograph, at other locations, similar instances of "slip bands" are visible but are not indicated as such. In their SE2 micrograph, two groups of slip bands are indicated—one of them appears dark and the other one bright. The surrounding areas show narrow twins that look similar to what is indicated as slip bands. A BSD image and a higher resolution could be of assistance in resolving this uncertainty, as EBSD colorized images and SE2 images only allow for a vague assumption. In some regions of the specimens in this thesis, local orientation changes could be identified after cyclic testing. These were concentrated to one, sometimes a few grains. The irregularities are best described as narrow lines of about 10 µm length. Their morphology reminded of a scratch in a soft material. However, these could be found in the images prior to testing as well and could therefore stem from sample preparation. This illustrates how useful the acquisition and stitching of pre- and post-testing images is and how it enables the exclusion of false positives in this case, without having to interrupt the testing. The surface marks are believed to be dislocations that traveled to the surface due to local deformation that was not removed with electropolishing or polishing artifacts. An exemplary image of two such irregularities can be found in the appendix (fig. A.3).

The microcrack found in neighboring grains of the slip bands in Ref. [18], appears very similar to microcracks of this thesis. The crack appears to be a approx. 50 µm long type I crack in the vicinity of a twin boundary with slip bands indicated parallel to the crack.

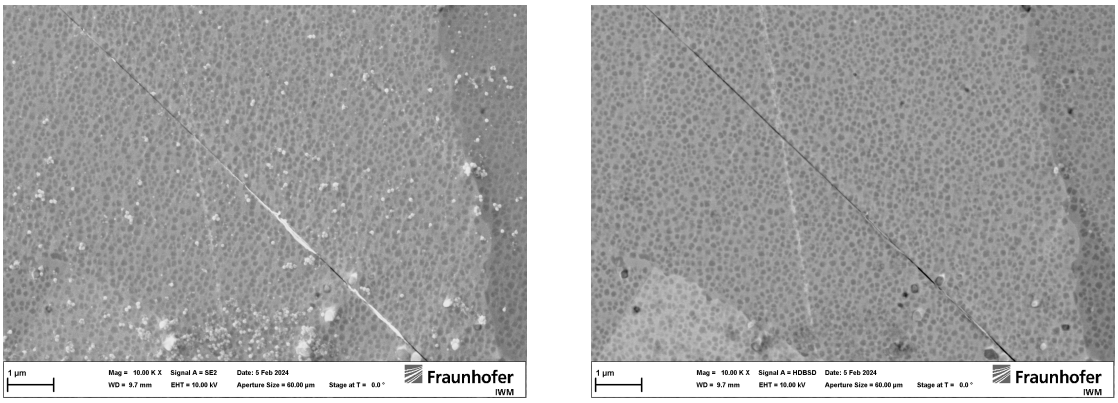

(a) (b)

Fig. 6.1 Comparison of the secondary electron (a) and the backscattered electron detector (b) for a microcrack. Secondary electrons are more surface sensitive (e.g., allow to image even thin extruded material), while the higher energy backscattered electrons emerge from deeper regions, making the thin extruded material transparent.

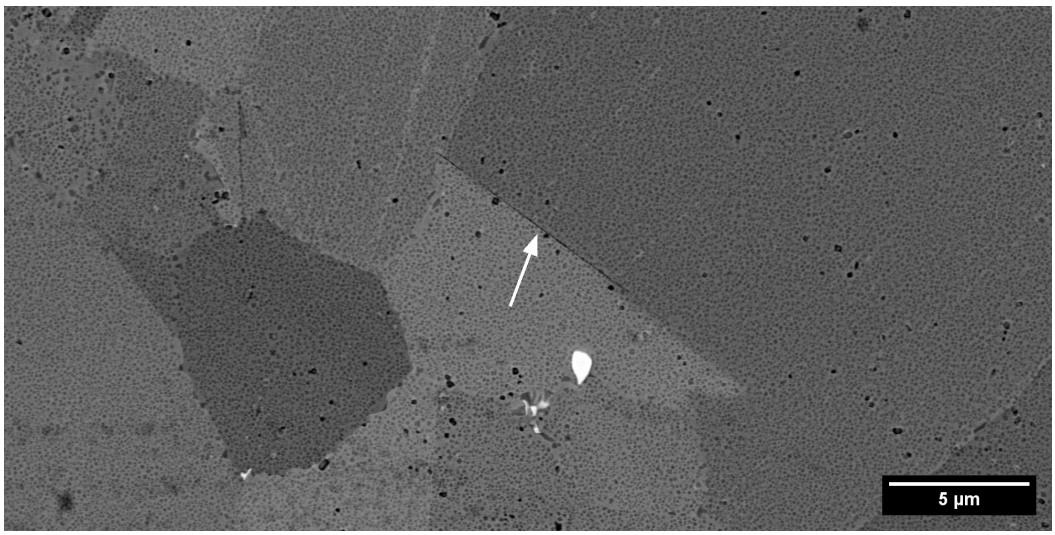

Fig. 6.2 An extremely fine microcrack near an incomplete TB, less than 10 µm long.

6.2 Microcrack initiation and crack propagation

6.2.1 Persistent slip bands as a precursor to crack initiation

Mughrabi [15] describes extrusions and intrusions as a necessary precursor for crack initiation. During the course of this thesis, including SE2 investigations, no extrusions or intrusions as a result of PSBs could be identified. One would think, if they really are precursors to fatigue

damage, at least some would have to be found as the scans include close to 100 cracks.[1] Slip bands were observed near cracks—parallel to or rotated by approx. 45-60 ° to the crack as in fig. 6.3 and as was observed in the crack propagation of the type IV crack in section 5.2.4. The nature of these bands is assumed to be related to fracture mechanics—the zigzag crack mode in this grain is similar to longer crack propagation found by Kuhn et al. [40] and unlike the crack initiation on slip systems like in fig. 6.2. This might be explained with information from Pippan and Weinhandl [48]. The observed "slip bands" at the crack tip are dislocations that are forming at the crack tip due to a local increase of stress intensity upon cyclic loading. This will culminate in the generation of a dislocation pair at the crack tip. The slip direction is in-plane and parallel along the slip band. During further loading, the dislocations move in the opposite direction of the crack until they reach their equilibrium position, where the local stress on the dislocation is equal to the friction stress and the stress at the tip increases again until another pair of dislocations is created. The spacing of these dislocations is the length of the Burgers vector [48].

The zigzag crack propagation is similar to the transition from stage I (shear crack propagation) to stage II (mode I-like propagation) of fatigue crack growth for low FCGRs. This transition occurs when the crack tip approaches piled-up dislocations at a GB. The shear stresses in front of the fracture decrease on the slip plane that it travels on and the shear stresses on a different nearby slip plane increase. This assists the dislocation generation on this new slip plane and causes the crack to deviate. A grain boundary providing high resistance against slip transmission[2] could initiate this transition already in the first grain, but sometimes a crack can propagate through a few grains before transitioning. How far this is affected by twins and twin boundaries is, however, not discussed in the paper.

Two instances of intense crack propagation (two locations from the same fatal crack) can be found in the appendix (fig. A.1 and fig. A.2). The multiple crack path deflection and rejoining even caused a piece to break out from the material.

[1] Including samples that were not included in table 4.1 and were seen as preliminary tests.

[2] It is assumed that a high resistance against slip transmission is associated with a HAGB.

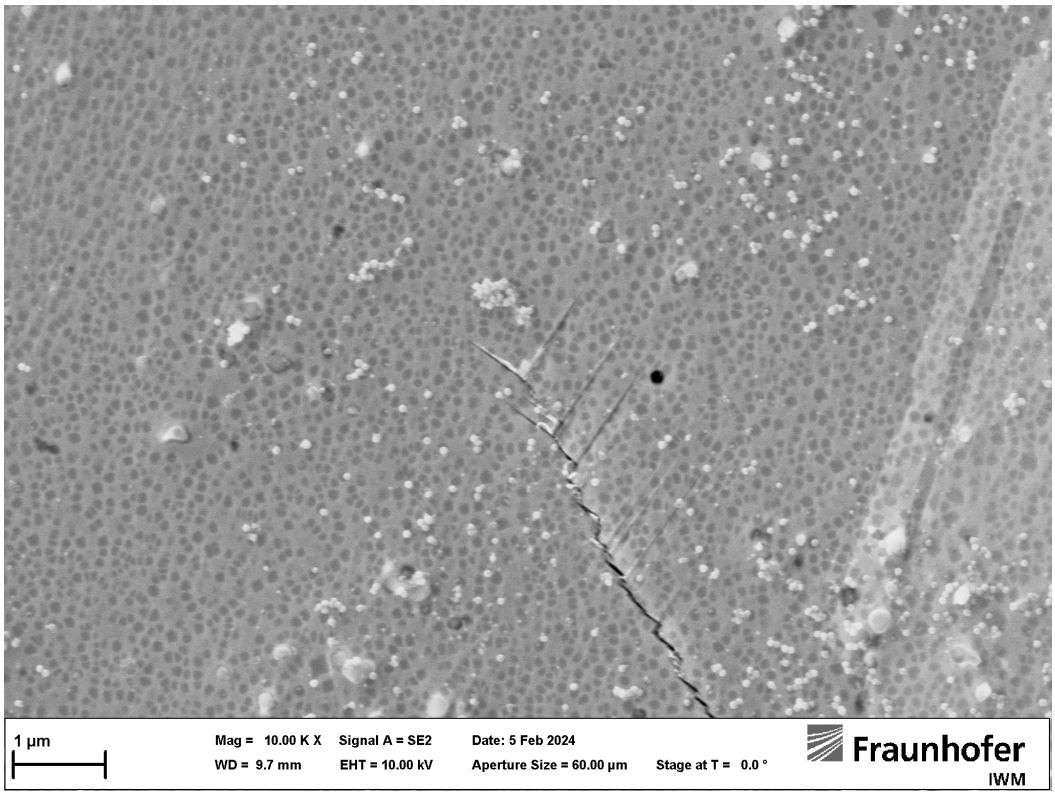

Fig. 6.3 The crack tip of a propagated type III crack with multiple slip bands parallel to each other (same slip system). The appearance is similar to illustrations of crack propagation from Weinahndl and Pippan [48].

6.2.2 Microcrack initiation in favorably oriented grains

From section 2.3, the important criteria for fatigue crack initiation have been identified as follows:

- Presence of a twin boundary. According to Charpagne et al. [17] the twin boundary surface area is the decisive factor for crack initiation, however, in 2D the twin boundary length is the important metric. A longer twin boundary is a statistically preferred crack initiation site compared to a shorter one. The dislocation motion along the TB and the pile-up of dislocations at an adjacent GB create a high stress field at the TB and TB/GB interface.

- High Schmid factor on a crystallographic plane in the twin and parent grain. The activated slip plane of a grain ought to be oriented for high SF and contain at least one twin. If more than one twin is present, crack initiation only occurs at one of them. Sometimes more than one plane is oriented for high shear stress and then slip may occur at a slip system that has a high SF but not necessarily the highest.

- Elastic modulus mismatch, ΔE_{LD}, between parent and twin grain. When the above criteria are satisfied, the difference in elastic modulus for the loading direction can create additional stress fields, favoring crack initiation. Below a certain combination of SF and ΔE_{LD}, no cracks initiate.

The SF and elastic modulus mismatch have been validated for macroscopic fully-reversed fatigue tests and simulations [13, 14, 17, 20–22, 30]. The paper of Alam et al. [18] also supports these criteria for fully-reversed bending resonance fatigue but questions remain about their setup and results because 80 MPa was not nearly enough to initiate cracks in this investigation and the calculation of the resonance frequency is not explained in detail. It is therefore not clear why fatigue damage resulted from much lower forces.

The microcrack initiation observed in this thesis was evaluated with respect to the aforementioned criteria. The results can be summarized as follows:

Twin boundary criterion: In this thesis, all valid cracks initiated parallel and close to a TB. The offset from the TB was not quantified but is estimated to be in the range of a few hundred nanometers. The TB length may be statistically influencing the crack initiation but many cracks started at rather short TBs. The position of the twin in the parent grain (complete, incomplete, corner, island [22]) was also not observed to have an influence on crack initiation, but very much so on propagation. The crack initiation sites were evaluated with the MTEX code from section 5.1.2 whether or not they are close to a TB. Crack propagation did not occur along TBs, except for the case in fig. 6.4, where the TB from an adjacent grain (IV-3 and 4) is almost an extension of the TB from the crack-initiating grain (IV-1 and 2). Additional statistics and quantitative analysis can be performed for this data set by applying a deep learning algorithm to segment cracks and correlate the grains where crack initiation occurred with EBSD data such as slip plane trace and slip direction for all cracks [49]. This could result in a more quantitative approach to correlate the microstructure with fatigue crack initiation. The utilization of TriBEAM femtosecond laser SEM is planned to be done on these samples to obtain an understanding of the three-dimensional processes influencing crack initiation and eventually more important, the propagation into higher order, and fatal fractures.

Schmid factor criterion: In the workflow the initiation sites of type I, II, III, IV cracks were evaluated with respect to their SF, the activated slip system (slip system with the highest SF, displayed by a trace of the plane), and the orientation of the Burgers vector (section 5.1.1).[3]

[3] The Burgers vector is parallel to the slip direction for the edge dislocations considered here.

This led to the following observations:

- Type I cracks were often found at island and incomplete TBs. The propagation of the crack was inhibited by the ending of the TB within the grain on one side. Due to the shorter length of the crack, it might not localize enough stress to overcome the GB at the other end. When the TB is complete (i.e. it reaches through the entire grain), crack initiation occurs along the whole length of the grain, the shear crack propagation has little resistance. However, if the twin ends within a grain and not at the grain boundary (in 2D), the elastic incompatibility is absent along with the twin boundary and crack propagation appears inhibited. An example can be seen in crack instance I-14 in fig. 6.5.

- Type II cracks did overcome one or two grain boundaries, but arrested in neighboring grains. It was observed that in these cases the activated slip systems of the neighboring grains differed and the grain boundary orientation was not found to have an effect on propagation. In case of a large deviation between the slip planes of two adjacent grains, crack deflection into other grains with more favorably aligned slip planes was often observed.

- Likewise for type III cracks, the slip systems of the crack initiating and neighboring grains were similarly oriented, allowing for easier propagation across the GB. This is very pronounced for the type IV crack of fig. 6.4. The initiating twin-parent pair (IV-1 and IV-2) both have high SF (dark red). The activated slip planes appear identical. The reason this crack propagated so quickly and grew across so many grains is attributed to the neighboring grain in yellow (i.e. IV-3, below the initiating grain). Here, a TB can be noticed which appears almost like an extension of the twin in the initiating grain, however, with a smaller SF. The crack from the high SF grain must have propagated very quickly to the similarly oriented grain. After that, the crack followed the activated slip planes of adjacent grains very closely. Additionally, a triple point is suspected in the initiating grain due to the blue line (also a twin) towards the top of the grain IV-1. The importance of triple junctions in fatigue crack initiation is pointed out by Charpagne et al. [17]. It was suggested that, “[...] the most intense and longest slip bands, which would become critical fatigue crack nucleation sites during cyclic loading, are located close and parallel to particular annealing twin boundaries and are simultaneously connected to triple junction lines.”

- The SF for all crack initiation sites was high (>0.43), independent of their propagation into a higher-order crack type.

During this thesis, a high Schmid factor was proven a necessity to initiate cracks—irrespective of their driving force to propagate—in line with previous investigations. However, the author noticed a generally high SF for all specimens and investigated the average SF for an area of 500 grains from AZI-1101-A-BR (nonmarked side). The arithmetic mean was determined with 0.456. The number of grains, that satisfy the criteria of high SF and the existence of a twin is hence quite large; of the 500 grains analyzed, 407 have a SF of 0.43 or higher. A histogram with a density curve of the SF distribution can be found in the appendix (fig. A.6). It clearly shows the maximum of the SF distribution at 0.48. One might argue, that if a crack initiates in a grain with SF=0.48, that this simply corresponds to the fact that a majority of grains is oriented similarly. It would therefore be extraordinary if a microcrack would form within a grain with a SF of e.g., 0.465.

Considering that a majority of grains has a high SF, the slip direction might be more relevant. In SF maps fig. 5.1d and fig. 6.4, no black arrow representing the Burgers vector/slip direction for an edge dislocation (black arrow) aligns with the trace of the activated slip plane (white line) on one side of the crack (grains II-2 and IV-2). This is understood, that the activated slip plane trace in this case is parallel to the axis of imaging (coming out of the plane) and the Burgers vector is absent because it is also parallel to the viewing direction and has therefore no components in-plane, only out of plane.[4] On the other side of the grain (grains II-1 and IV-1) the trace is also parallel to the twin boundary but there the slip direction is along the trace. This means that the components of the slip direction vector are almost exclusively in-plane. The slip directions of the two grains adjacent to the crack are therefore perpendicular to each other. The cracks formed in the grains with the in-plane Burgers vector (grains II-1 and IV-1).

In the EGM (Essmann, Gösele, Mughrabi) model [50] the slip plane is inclined 45 ° to the loading direction, and the slip direction is solely in-plane, parallel to the slip plane, e.g., $(1\,1\,1)$ $[0\,\bar{1}\,1]$. Dislocation motion along the slip plane leads to the creation of extrusions (swelling due to annihilation of opposite sign vacancy-type edge dislocations and consequent vacancy generation) and intrusions (annihilation of interstitial-type dipoles) on the left and right surface of the specimen but not on the surface, which is on the front [15]. If a crack forms at the extrusion-intrusion pairs, it would be perpendicular to the loading direction.

If the crack is under a 45 ° angle to the loading direction, like it is the case in this investigation, the trace of the slip plane would then have to be also 45 ° inclined to the loading direction, and the projection of the Burgers vector perpendicular to the trace and coming out of plane. This is not the case.

[4] Burgers vector may equivalently also be into plane.

As mentioned above, the slip direction is parallel to the trace of the slip plane and not out of the plane. The dislocations would then travel parallel to the TB (until they reach the neighboring GBs). This would explain why no extrusions or intrusions were found on the surface.

If the model from Tanaka, Mura, and Venkataraman is correct (see section 2.2.3), the positive dislocations may move in one direction during tensile loading and the negative dislocations in the opposite direction during compressive loading. Both types of dislocations run on distinctively spaced slip planes but are still part of the same slip band in a planar surface grain of a polycrystalline material. In their micromechanical model, this leads to a dislocation pile-up of (positive and negative) vacancy-type dislocations on one side and interstitial-type dislocations on the other side. Chan [51] expanded their model and showed that an increasing number of cycles can be linked to a change in Gibbs free energy and that once a maximum is reached—and the surface energy-barrier is overcome—the crack initiates. The crack length, however, is not always equal to the length of the slip band. The model uses the number of dislocations that are necessary to create a strain-energy density greater than the surface energy to connect fatigue cycles and crack length. Chan refers to this approach as a crack size-based fatigue-crack-initiation model. The equation for the initiation of a fatigue crack can be found in Ref. [51]. The model was found to fit well with the experimental data for PM Astroloy (nickel-based superalloy with high contents of cobalt and chromium), which is also a material used for disks in aircraft engines.

The observation of many microcracks in this thesis are in line with the model; microcrack initiation occurs solely on the slip planes with the highest resolved shear stress, and the slip direction vector is often planar and parallel to the slip plane. The absence of fatigue-induced surface roughness is also explained by this model. Stinville et al. [13, 41] also report cracks under a 45-60 ° angle to the loading direction in rotationally symmetrical specimens in axial push-pull fatigue tests. What is not specifically answered from this model is the application to incomplete and island twins, which were seen to initiate microcracks frequently in this thesis. Maybe it is possible that the ending of a twin grain within a parent grain has a similar effect as a GB.

Elastic modulus mismatch: The ΔE_{LD} analysis is not implemented in MTEX and was therefore not further investigated apart from some local analysis with the OIM software, that did not seem to contradict previous results.

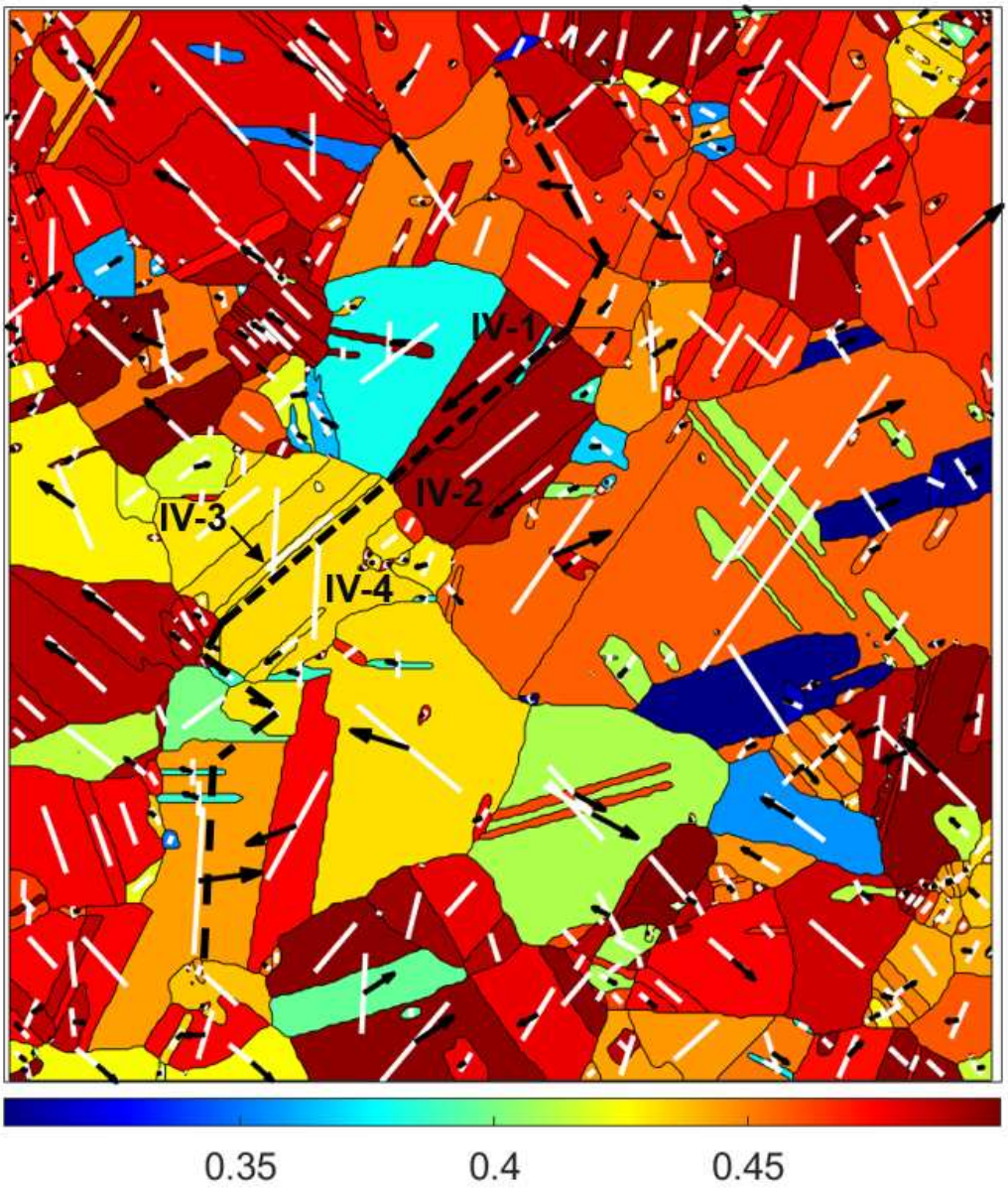

Fig. 6.4 Schmid factor map (unitless) of a type IV crack from sample AZI-1101-A-BR, indicating the crack path with a black dashed line. The crack initiated close to the TB of grains IV-1 and IV-2 and then propagated along the TB of grains IV-3 and IV-4. The numbering is arbitrary. Crack propagation occurs along the activated slip planes of the grains, respectively.

6.2.3 Grain cluster investigation and crack arrest at HAGBs

The grain cluster hypothesis from Miao et al. [30] states that "Grain boundaries with a low misorientation (LAGB) are more facile for cracks to propagate across than GBs with a high misorientation (HAGB[5]). Cracks grow preferentially in grain clusters of such low misorientation and cracks are shown to arrest at HAGBs surrounding the cluster."

However, to the best of the author's knowledge, the grain cluster hypothesis has not been validated since the initial efforts of Miao, Pollock, and Jones [30]. Furthermore, the Rene'88DT samples from this investigation were likely produced in 2007. It is not ruled out that the material has been altered since then—either in the PM process or in the heat treatment process.

This hypothesis was tested for multiple crack initiation sites and it can be summarized that no correlation as stated in the paper cited above was found. In fig. 6.5 a grain cluster map was plotted, colorized as a function of area size, and it is evident that the cracks number I-11, 12, 13, 14, and 16 arrest somewhere within the grain cluster. As stated in section 6.2.2, the governing factor for the arrest of a crack seems to be the twin boundary. One could argue, that this grain cluster hypothesis is designed for cracks that propagate and overcome at least one LAGB. This, however, was also not confirmed. The type IV crack from fig. 6.4 arrested, in the end, at two HAGBs, but it first overcame four of them. Another type III crack initiated at a TB (fig. A.5 grains III-1 and III-2) and propagated to the top and towards the bottom to about equal distance. In the top part the crack remained in one cluster and arrested eventually when the crack tip split up into three paths, propagated a few microns on each and then it stopped. The bottom part of the crack overcame the first HAGB right at the TB-HAGB-junction, then propagated through a few small grains with HAGBs, before reaching a larger cluster again. Then it propagated on the activated slip plane before it was deflected at a TB, which it followed to the HAGB. The crack followed the GB for a while before passing through another HAGB and eventually, it arrested within this grain. To conclude, neither the top section arrested at a HAGB nor the bottom part of the crack.

The hypothesis was therefore not validated in this thesis and to the author's knowledge, no other research team has yet been able to confirm it. Hence, the results from Miao may not reflect a general principle for short crack propagation in nickel-based superalloy Rene'88DT. However, the setup was different in their investigation; they used cylindrical specimens with frequencies more than ten times higher than in this investigation .

What was interesting to be observed for this aforementioned type III crack is the crack propagation path of the top part of the crack (fig. A.5). After leaving the TB (between grains

[5] In this hypothesis, a HAGB is defined as a GB with a misorientation angle greater than 20 °, unlike in Ref. [24], where the threshold is defined as 15 °.

III-1 and III-2) it progresses through parts of a grain with low SF (grain III-3). Instead of continuing on the activated slip plane, like the type IV crack did in the orange grain at the bottom in fig. 6.4, it changes direction and slip plane to propagate toward a region of grains with high SF.

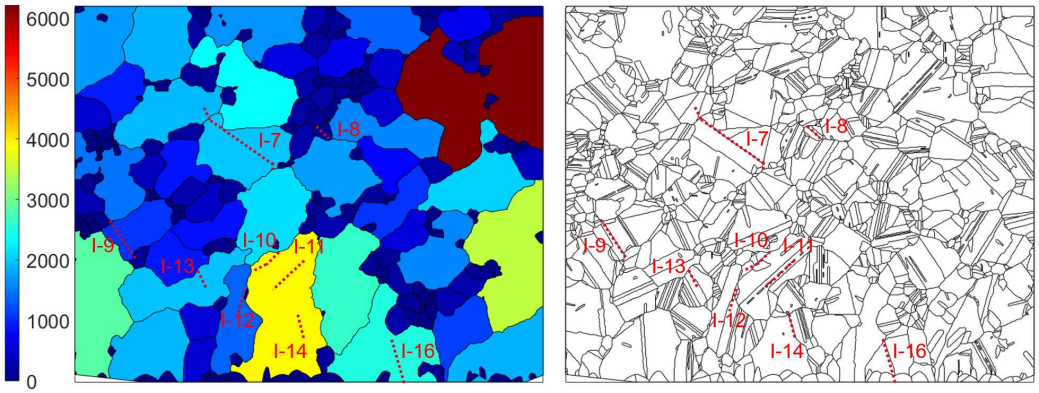

Fig. 6.5 Grain cluster map as a function of area size in μm^2 (left) and grain boundary map (right) with indications of nine type I cracks from sample AZI-1106-A-BR nonmarked side. Grain clusters are constituted of grains having a misorientation angle smaller than 20 ° and were merged as described in section 5.1.3.

6.3 Plastic strain evaluation with HRDIC and HDIC

The absence of intrusions and extrusions, and essentially any slip markings, necessitated a qualitative evaluation of microstrain in the regions of microcrack initiation. The main goal was to gain further insights into the crack initiation process, to compare results with theories like the EGM model [50] or the extended model of Tanaka, Mura, Venkataraman by Chan [51], and to compare the free and open-source software µDIC to not publicly available programs such as Heaviside DIC (see also section 5.2). Different (sections of) cracks were examined with µDIC based on the images from the large area scans. In some areas, the amounts of extruded material made an image correlation impossible, in other areas, the automated image capturing led to differences in focus and the image resolution of the γ' was therefore too different in the before and after image to allow for a valid correlation. Another issue was related to the backscattered electron detector; the orientation contrast, which leads to the different grey values in different grains, changes with even a slight change in specimen orientation. The workflow did not consider this and so the specimens were tested in a different sample holder than they were imaged in before the test (to save time). This caused a different grey value in some grains/twins in images before and after testing due to deviations with the sample holder clamping.

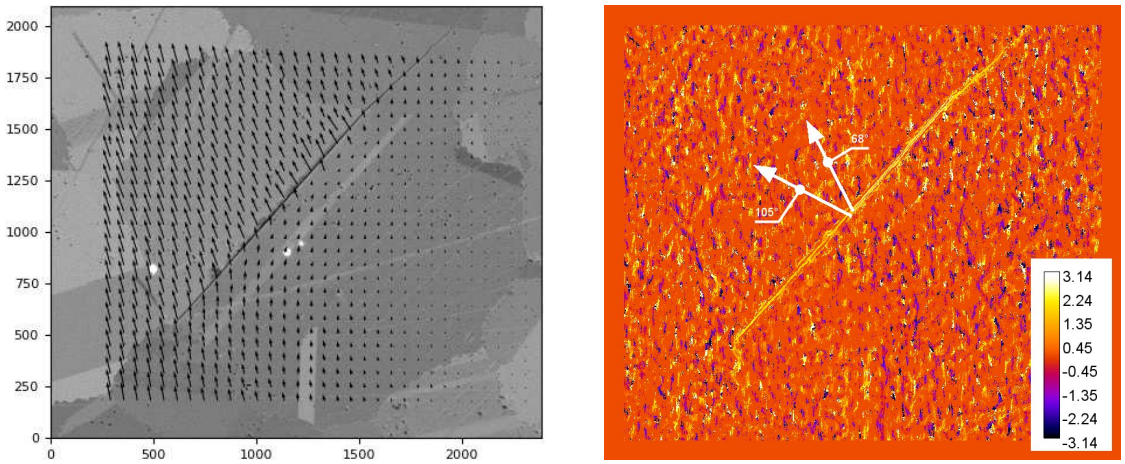

(a) (b)

Fig. 6.6 a) µDIC quiver plot showing the displacement of the discrete points by arrows which are scaled for visibility. The registration was performed on the right side of the image, towards the clamped side. A clear change of the direction of the displacement and its magnitude can be observed close to the crack pointing towards the top left corner of the image indicating a shear and slide displacement. The axes are in pixels, a conversion to nanometers can be found in the appendix; b) The angle of displacement γ as generated with HDIC. The location of the crack and the input images were identical to fig. 6.6a. The legend (in radians) identifies the displacement angle at the crack between 68 ° and 105 ° (see section 5.2.4). The almost regular pattern in the rest of the image is considered noise.

The HRDIC led to interesting results for the type II crack (fig. 6.6a, see also fig. 5.1 for IPF, TB, SF, and GC maps). The displacement of the 832 individual points of the finite element discretization is displayed with vectors that are scaled for visibility. The right side of the image shows little to no distortion and this can be attributed to the image registration that was done in this region. At the crack, the highest displacements are recorded, but also a change in direction—moving up and left—is apparent, indicating a sliding displacement (i.e. displacement perpendicular to the crack direction). Further left from the crack, a uniform displacement to the top left corner is discernible, probably because of a deformation of the entire area due to the crack opening displacement. The vector plot indicates a sliding and opening of the left side of the crack towards the unclamped, free-swinging end of the specimen. Some neighboring grains on the left side appear to be affected as well.

The direct comparison with the Heaviside DIC (fig. 6.6b) shows that the angle of displacement is similar in both analyses. The angle of displacement in the HDIC was obtained from the values in the image and varies between 68 ° and 105 ° for the area of the crack (orange line). The HDIC angle γ represents the inclination of the accumulated in-plane slip vector and the slip plane trace is between $\pm 0 - 180$ where 0 ° and 180 ° correspond to pure in-plane shearing and 90° to pure in-plane sliding. The displacement in this grain is

therefore mostly sliding. Bourdin et al. [47] also describe an accumulated Burgers vector that "represents the magnitude and direction of the shearing in the gliding plane that results from accumulated lattice distortion caused by dislocations emerging at the surface of the material along a given slip plane." This paper however only deals with macroscopic tensile tests and not fatigue tests. The evaluation is done on slip bands from a high plastic loading which emerge when dislocations move to the surface of the specimen during tensile tests. The trace of the slip planes is shown in the images, but the Burgers vector of the slip planes is not. With the model from Tanaka, Mura, and Venkataraman [27] for cyclic loading fatigue crack initiation, dislocations do not emerge on the surface but move along it. It is therefore unclear to the author how this accumulated Burgers vector is responsible for cracks that do not stem from dislocation surface steps. The author would argue that the displacement at the crack is created by the lattice distortion that occurs following the crack initiation from the Gibbs free energy criterion of Chan. As was shown by Stinville et al. [41], the tensile strain (ε_{xx}) at a fatigue crack can reach up to 12 % (evaluated with HRDIC). An opening up of the crack, in a direction perpendicular to the crack, to relieve the tensile strain could therefore be a reason for the mostly sliding displacement observed. Further tests have to be made to validate this hypothesis.

In summary, the HRDIC with µDIC was a successful first proof of concept, as it was shown to work with the inherent, unetched pattern of the γ' precipitates and ex-situ pre- and post-testing scans at $3,000\times$ magnification. The displacement in fig. 6.6a was validated with GOM correlate, another software for image correlation. The minimum feasible distance between discrete element points was found to be around 65 pixels ($\widehat{=}$ 1.2 µm) for this data set. The strain can be displayed as true strain in a contour plot, but the calculation of the true strain was not specified in the paper, and therefore the created analyses were not used in this thesis [46]. The displacement visualization with vectors was chosen for convenient interpretation and no modifications were necessary. However, it could be valuable to additionally read out the displacement values for single points, and this could be done with amendments to the code.

Some questions remain regarding the image registration with the GUI selecting points on the pre and post scans. Even though the point selection was very accurate, the affine transformation may not lead to the desired results for HRDIC and may introduce adverse effects. Additionally, the ex-situ imaging can lead to issues with stage repeatability, drift, noise, and focus. The latter one was particularly pronounced for this investigation as the DIC images were taken from the large-area scans, which were taken without refocusing every single image composing the large area. The middle of the scan area was focused once and the same imaging parameters were used for the entire area. Sometimes the samples were

not absolutely plane-parallel and so some sections were not fully in focus. This choice was made as focusing every single image would have increased acquisition time significantly. Furthermore, the focussing on a smaller area in the current imaging frame led to dark spots in the BSD image, causing problems with DIC. This was not a problem with SE2 detector but for BSD. Alternative ways to calibrate ex-situ DIC may enhance the denoising of the data and an even smaller point spacing could be achieved. Such calibrations involve elaborate pattern application on sample surfaces and programming corrections for the spatial distortion in the SEM [44].

Chapter 7

Summary and conclusions

The trend towards higher rotational speeds, greater fuel efficiency, longer service interval periods, and the improvement of multidimensional material models for cyclic loading necessitates a better understanding of key factors governing the initiation and propagation of cracks. The complex combination of the applied loads, the high temperature, and the structure of the polycrystalline material containing twins and precipitates, increase the difficulty to predict weak points and to improve the microstructure to reduce fatigue-induced damage. This work extends previous investigations obtained on macroscopic axial fully-reversed tests by bending resonance fatigue tests with mesoscaled specimens using nickel-based superalloy Rene'88DT. The application of materials data analysis with the open-source programs MTEX (Matlab) and μDIC (Python) allows to extract crystallographic properties of grains where crack initiation occurred and to connect them to sub-grain plastic deformations.

This was made possible by a thorough specimen preparation process including grinding and chemo-mechanical polishing, as well as electropolishing to remove residual deformation layers and stress concentrations at corners. This involved a custom-built setup with a LABView program for electropolishing of samples with a length of about 16 mm in an acidic electrolyte and mounting the mesoscaled samples onto steel cylinders for grinding in conventional rotational devices.

After preparation, both sides of the sample were imaged in a SEM using a high-definition backscatter electron detector (HDBSD) and an electron backscatter diffraction (EBSD) scan to obtain information about the crystallographic orientation of the grains. The HDBSD images taken at $3,000\times$ magnification were stitched together using free software to document the initial state of the samples before testing. This proved valuable in the identification of what appeared to be slip bands that traveled to the surface and justified the image acquisition time of about eight hours per scan. SEM corrections following Mello et. al [44] were applied to improve image quality and to reduce impeding effects of SEM imaging.

With a FE analysis, the applied stress was converted into the necessary parameters of the bending resonance device, and the resonance frequency was estimated. The applied von Mises stress was varied between 300 and 450 MPa for the relevant tests. The bending resonance fatigue setup utilizes two in-phase piezo actuators at the top in the clamped section, while the free end of the sample (referred to as mass) swings back and forth at the resonance frequency, deflecting a laser beam onto a position-sensitive device. Deviations of the frequency can be registered and are a sign of fatigue damage in the specimen. Additionally, a camera capturing darkfield images is installed, to observe one surface of the sample in situ. This enables to manually stop the experiment when damage accumulates on the surface and allows to extract the number of cycles to initiate a crack. A total of 45 cracks due to microstructural factors were counted in four specimens, 64 % of them were constrained to one grain (type I crack). Twelve cracks, that started at an edge or a pore, were excluded from this analysis. However, it shows how detrimental such defects are for fatigue crack initiation. The specimens were not fatigued until failure, but the tests were stopped after a few cracks could be observed on the surface, as the aim was not the determination of a Wöhler curve, but the investigation of microcrack initiation and propagation and to relate them to the (local) microstructure. With an increasing number of cycles, some of these short cracks would have propagated further.

After fatigue testing, the specimens were imaged again using identical SEM settings as prior to testing to acquire the necessary images to identify crack initiation locations and to select ROIs for HRDIC.

The HDBSD images displayed a superior contrast between individual grains and the inherent γ' precipitates with about 100–200 nm size. Along with the elaborate specimen preparation, this ensured high-quality surfaces and the successful application of HRDIC on these images. The use of HRDIC was necessary as preliminary tests revealed no slip markings or other indications of local plastic strain. With the HRDIC, the displacements at cracks could be displayed semi-quantitatively. The EBSD scans were evaluated with MTEX for microstructural properties such as Schmid factor of grains, grain boundary misorientation, and twin boundaries, to correlate early fatigue damage with the (local) microstructure, and to display it in 2D plots.

At crack initiation sites, no signs of intrusions or extrusions could be observed. Sometimes, extruded material is present at the crack opening—especially for higher order type cracks (III and IV)—which may be the result of friction within the crack during continued cycling loading. However, it does not appear that crack initiation is caused by the formation of intrusions and extrusions following the EGM (Essmann, Gösele, Mughrabi) model [50]. This is supported by Schmid factor maps depicting the traces of the corresponding activated slip plane and slip direction; in many instances the Burgers vector is (nearly) solely in-plane,

causing a dislocation movement in-plane, but not out-of-plane, assumed to be unable to create surface roughness, e.g., intrusions and extrusions. Therefore, the EGM model [50] does not appear to be suitable to describe the initiation of microcracks at the surface of bending resonance fatigue specimens. Instead, the slip band cracking model of Chan [51], following the efforts of Tanaka, Mura, and Venkataraman [27], is better suited for the present fatigue crack observations. The model describes the dislocation movement on two separate, but very closely spaced, planes within a slip band. The pile-up of (positive and negative) vacancy-type dislocations and (positive and negative) interstitial-type dislocations at the grain boundaries on either end of the slip band, creates unfavorable changes in the Gibbs free energy. Once the surface energy-barrier is overcome, fracture initiates along the entire slip band. The necessary number of cycles can be calculated following Chan's formula and in the publication, it was found to fit empirical data of fatigue tests on steel, nickel- and titanium-based alloys well [51].

References

[1] Biswas S, Ramachandra S, Hans P, Kumar SPS. Materials for gas turbine engines: present status, future trends and indigenous efforts. Journal of the Indian Institute of Science. 2022;102(1):297-309.

[2] Krueger DD, Kissinger RD, Menzies RG. Development and introduction of a damage tolerant high temperature nickel-base disk alloy. Superalloys. 1992:277-86.

[3] King T, Hurchalla J, Nethaway D. United States Air Force engine damage tolerance requirements. In: 21st Joint Propulsion Conference. Monterey, CA, USA; 1985. p. 1209.

[4] Buk J, Sułkowicz P, Szeliga D. The Review of Current and Proposed Methods of Manufacturing Fir Tree Slots of Turbine Aero Engine Discs. Materials. 2023;16(14):5143.

[5] Prasad NE, Wanhill RJH. Aerospace materials and material technologies. vol. 1. Springer; 2017.

[6] Gessinger G. Powder Metallurgy of Superalloys. 1st ed. Butterworth-Heinemann; 1984.

[7] Wlodek ST, Kelly M, Alden DA. The structure of Rene 88 DT. Superalloys. 1996:129-36.

[8] Caillard D, Molénat G, Paidar V. On the role of incomplete Kear-Wilsdorf locks in the yield stress anomaly of Ni_3Al. Materials Science and Engineering: A. 1997;234:695-8.

[9] Ru Y, Zhao H, Zhang H, Pan X, Zhao W, Pei Y, et al. Design for anomalous yield in γ-strengthening superalloys. Materials & Design. 2019;183:108082.

[10] Antolovich SD. Microstructural aspects of fatigue in Ni-base superalloys. Philosophical Transactions of the Royal Society A: Mathematical, Physical and Engineering Sciences. 2015;373(2038):20140128.

[11] Suresh S. Fatigue of materials. Cambridge University Press; 1998.

[12] Stinville JC, Charpagne MA, Cervellon A, Hemery S, Wang F, Callahan PG, et al. On the origins of fatigue strength in crystalline metallic materials. Science. 2022;377(6610):1065-71.

[13] Stinville JC, Lenthe WC, Echlin MP, Callahan PG, Texier D, Pollock TM. Microstructural statistics for fatigue crack initiation in polycrystalline nickel-base superalloys. International Journal of Fracture. 2017;208:221-40.

[14] Pinz M, Weber G, Stinville JC, Pollock T, Ghosh S. Data-driven Bayesian model-based prediction of fatigue crack nucleation in Ni-based superalloys. npj Computational Materials. 2022;8(1):39.

[15] Mughrabi H. Cyclic slip irreversibilities and the evolution of fatigue damage. Metallurgical and Materials Transactions B. 2009;40:431-53.

[16] Straub T, Berwind MF, Kennerknecht T, Lapusta Y, Eberl C. Small-scale multiaxial setup for damage detection into the very high cycle fatigue regime. Experimental Mechanics. 2015;55:1285-99.

[17] Charpagne MA, Hestroffer JM, Polonsky AT, Echlin MP, Texier D, Valle V, et al. Slip localization in Inconel 718: a three-dimensional and statistical perspective. Acta Materialia. 2021;215:117037.

[18] Alam Z, Eastman D, Weber G, Ghosh S, Hemker K. Microstructural aspects of fatigue crack initiation and short crack growth in René 88DT. In: Superalloys 2016: proceedings of the 13th international symposium of Superalloys. Wiley, Hoboken. Seven Springs, PA, USA; 2016. p. 561-8.

[19] Caton MJ, Jha SK, Rosenberger AH, Larsen JM. Divergence of mechanisms and the effect on the fatigue life variability of Rene'88DT. Superalloys. 2004:305-12.

[20] Stinville JC, Lenthe WC, Miao J, Pollock TM. A combined grain scale elastic–plastic criterion for identification of fatigue crack initiation sites in a twin containing polycrystalline nickel-base superalloy. Acta Materialia. 2016;103:461-73.

[21] Zhang X, Dunne FP. Short crack propagation near coherent twin boundaries in nickel-based superalloy. International Journal of Fatigue. 2023;172:107586.

[22] Lenthe WC, Echlin MP, Stinville JC, De Graef M, Pollock TM. Twin related domain networks in René 88DT. Materials Characterization. 2020;165:110365.

[23] Zhao M, Wu T, Zhao Z, Liu L, Luo G, Chen W. Ultrasonic fatigue device and behavior of high-temperature superalloy Inconel 718 with self-heating phenomenon. Applied Sciences. 2020;10(23):8761.

[24] Gottstein G. Physical foundations of materials science. vol. 3. Springer; 2004.

[25] Schmid E, Boas W. Plasticity of crystals. F.A. Hughes & Co. Limited; 1950.

[26] Lukáš P, Kunz L. Role of persistent slip bands in fatigue. Philosophical magazine. 2004;84(3-5):317-30.

[27] Venkataraman G, Chung Y, Mura T. Application of minimum energy formalism in a multiple slip band model for fatigue—II. Crack nucleation and derivation of a generalised Coffin-Manson law. Acta Metallurgica et Materialia. 1991;39(11):2631-8.

[28] Hestroffer JM, Latypov MI, Stinville JC, Charpagne MA, Valle V, Miller MP, et al. Development of grain-scale slip activity and lattice rotation fields in Inconel 718. Acta Materialia. 2022;226:117627.

[29] Bataille A, Magnin T. Surface damage accumulation in low-cycle fatigue: physical analysis and numerical modelling. Acta metallurgica et materialia. 1994;42(11):3817-25.

[30] Miao J, Pollock TM, Jones JW. Microstructural extremes and the transition from fatigue crack initiation to small crack growth in a polycrystalline nickel-base superalloy. Acta Materialia. 2012;60(6-7):2840-54.

[31] DIN 50100:2022-12: Load controlled fatigue testing - Execution and evaluation of cyclic tests at constant load amplitudes on metallic specimens and components [Standard]; 2022.

[32] Vander Voort G, Manilova E, Lucas GM. Metallographic techniques for superalloys. Microscopy and Microanalysis. 2004;10(S02):690-1.

[33] Shrivastava A, Kumar SA, Nagesha BK, Suresh TN. Electropolishing of Inconel 718 manufactured by laser powder bed fusion: Effect of heat treatment on hardness, 3D surface topography and material ratio curve. Optics & Laser Technology. 2021;144:107448.

[34] Goldstein JI, Newbury DE, Michael JR, Ritchie NWM, Scott JHJ, Joy DC. In: Backscattered Electrons. Springer; 2017. p. 15-28.

[35] Durmaz AR, Hadzic N, Straub T, Eberl C, Gumbsch P. Efficient experimental and data-centered workflow for microstructure-based fatigue data: towards a data basis for predictive AI models. Experimental Mechanics. 2021;61:1489-502.

[36] Shyam A, Torbet CJ, Jha SK, Larsen JM, Caton MJ, Szczepanski CJ, et al. Development of ultrasonic fatigue for rapid, high temperature fatigue studies in turbine engine materials. Superalloys 2004. 2004:259-68.

[37] Cowles BA. High cycle fatigue in aircraft gas turbines—an industry perspective. International Journal of Fracture. 1996;80:147-63.

[38] Zhang ZJ, Li LL, Zhang P, Zhang ZF. Fatigue cracking at twin boundary: effect of dislocation reactions. Applied Physics Letters. 2012;101(1):011907.

[39] Jiang R, Song YD, Reed PA. Fatigue crack growth mechanisms in powder metallurgy Ni-based superalloys—A review. International Journal of Fatigue. 2020;141:105887.

[40] Kuhn F, Zeismann F, Brückner-Foit A, Kadau K, Gravett P. Crack paths in the superalloy IN738 in aged conditions. Engineering Fracture Mechanics. 2013;108:275-84.

[41] Stinville JC, Vanderesse N, Bridier F, Bocher P, Pollock TM. High resolution mapping of strain localization near twin boundaries in a nickel-based superalloy. Acta Materialia. 2015;98:29-42.

[42] Kammers AD, Daly S. Self-assembled nanoparticle surface patterning for improved digital image correlation in a scanning electron microscope. Experimental Mechanics. 2013;53:1333-41.

[43] Pinard PT. Quality metrics; 2011. Date accessed: 2024-05-29. https://ebsd-image.readthedocs.io/en/latest/documentation/reference/qualitymetrics.html.

[44] Mello AW, Book TA, Nicolas A, Otto SE, Gilpin CJ, Sangid MD. Distortion correction protocol for digital image correlation after scanning electron microscopy: emphasis on long duration and ex-situ experiments. Experimental Mechanics. 2017;57:1395-409.

[45] Module ITK Transform; 2024. Date accessed: 2024-04-02. https://itk.org/Doxygen/html/classitk_1_1AffineTransform.html.

[46] Olufsen SN, Andersen ME, Fagerholt E. μDIC: An open-source toolkit for digital image correlation. SoftwareX. 2020;11:100391.

[47] Bourdin F, Stinville JC, Echlin MP, Callahan PG, Lenthe WC, Torbet CJ, et al. Measurements of plastic localization by heaviside-digital image correlation. Acta Materialia. 2018;157:307-25.

[48] Pippan R, Weinhandl H. Discrete dislocation modelling of near threshold fatigue crack propagation. International Journal of Fatigue. 2010;32(9):1503-10.

[49] Thomas A, Durmaz AR, Straub T, Eberl C. Automated quantitative analyses of fatigue-induced surface damage by deep learning. Materials. 2020;13(15):3298.

[50] Essmann U, Gösele U, Mughrabi H. A model of extrusions and intrusions in fatigued metals I. Point-defect production and the growth of extrusions. Philosophical Magazine. 1981;44:405-26.

[51] Chan KS. A microstructure-based fatigue-crack-initiation model. Metallurgical and Materials Transactions A. 2003;34:43-58.

Appendix A

Appendix

The settings for the BSD and EBSD scans were the same for all large-area scans and if not stated otherwise can be converted with the following table:

	Pixel	Nanometer
BSD	1	18.61
EBSD	1	500

Table A.1 Conversion table for pixel into nm for BSD and EBSD.

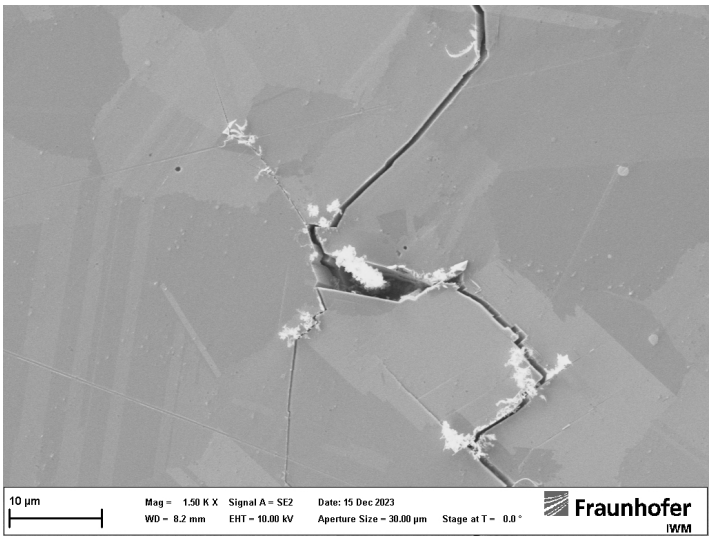

Fig. A.1 Closeup of a crack propagating through several grains, changing slip systems, and rejoining again. Interesting is the information that the material cracked also beneath the surface creating something like steps. This once again shows how complex crack propagation is. Same crack and sample as in fig. A.2.

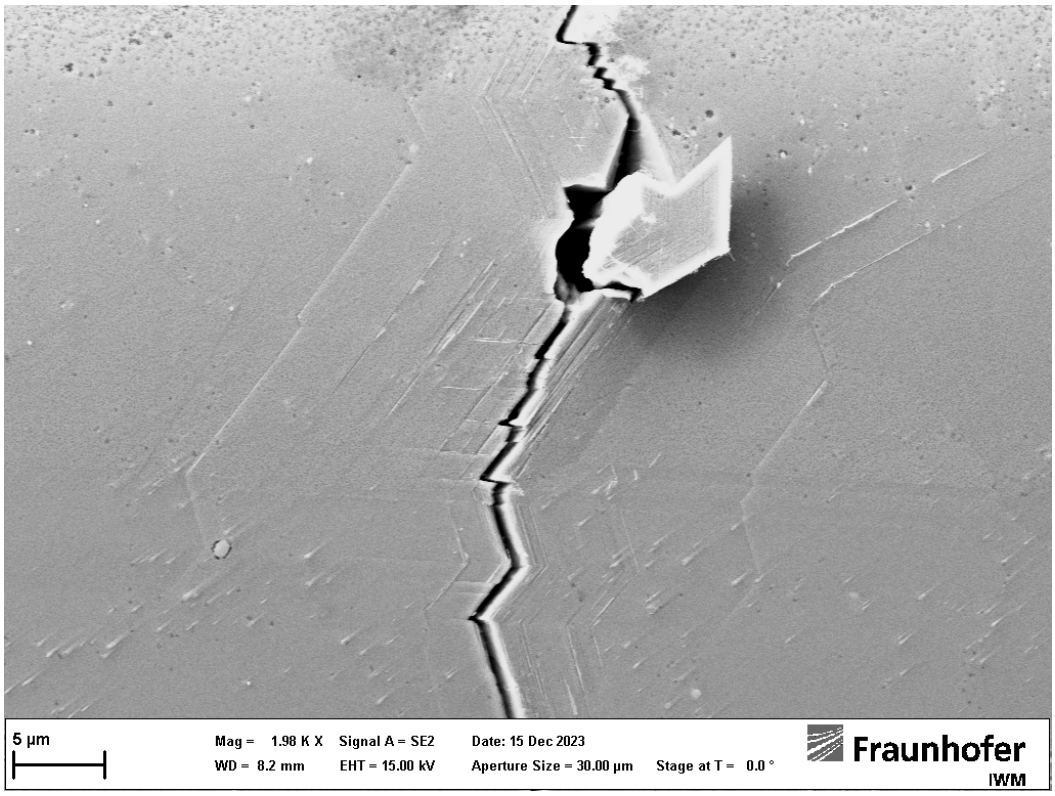

Fig. A.2 This SE2 micrograph from the fatal crack of a preliminary test with specimen AZI-1103-A-BR (see also fig. 3.4) toward the top of the gauge section of the marked side. Clearly visible are parallel activated slip systems to the crack path and some microcracks with some form of extruded material in the vicinity.

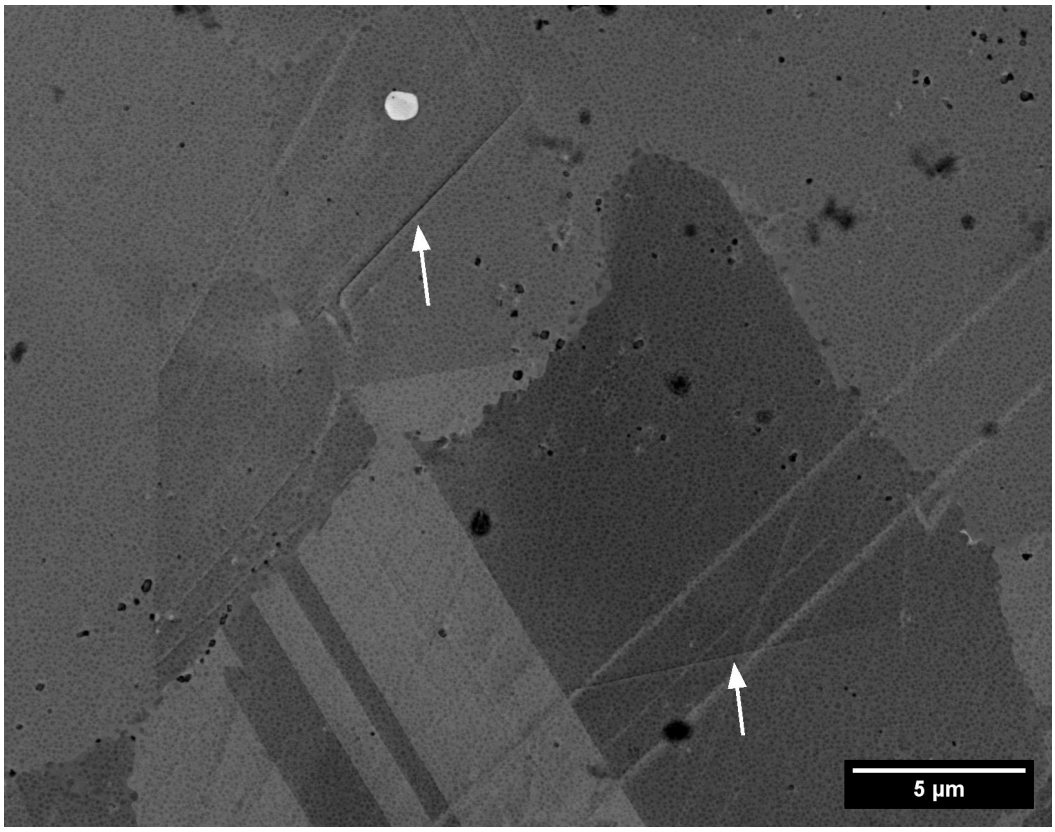

Fig. A.3 The figure shows a selection of the post-testing large area BSD scan with two abnormalities in two different grains with no parallel orientation to a TB (indicated with arrow). The "slip bands" appear to be the result of local plastic deformation, possibly during specimen preparation, because the bands were also found on the pre-testing scans. They are not scratches.

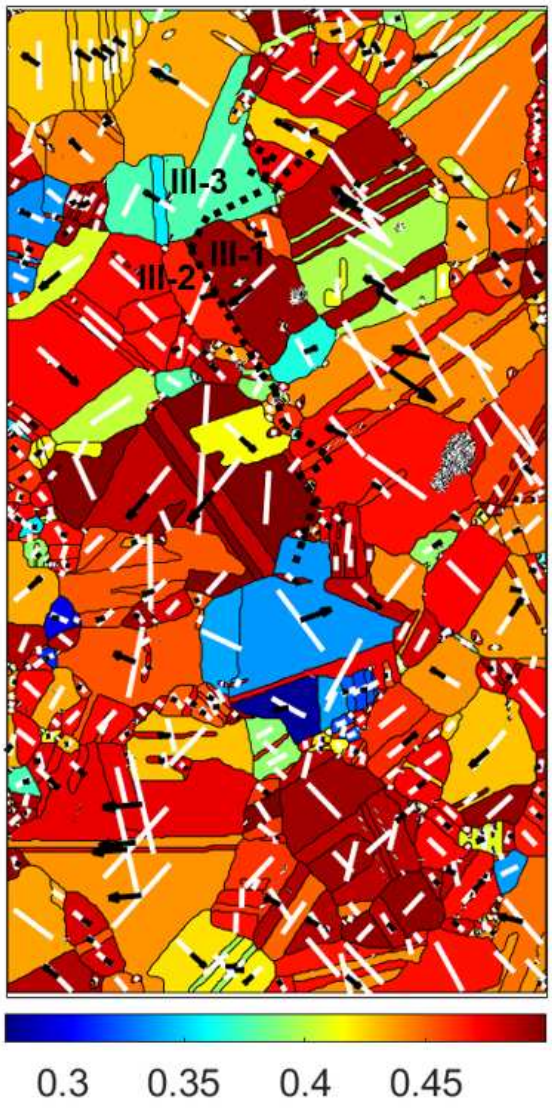

Fig. A.4 Schmid factor map (unitless) with activated slip plane trace (white) and Burgers vector (black arrow) and an annotation of the crack propagation path with a black dashed line. The crack initiated near the TB of grains III-1 and III-2.

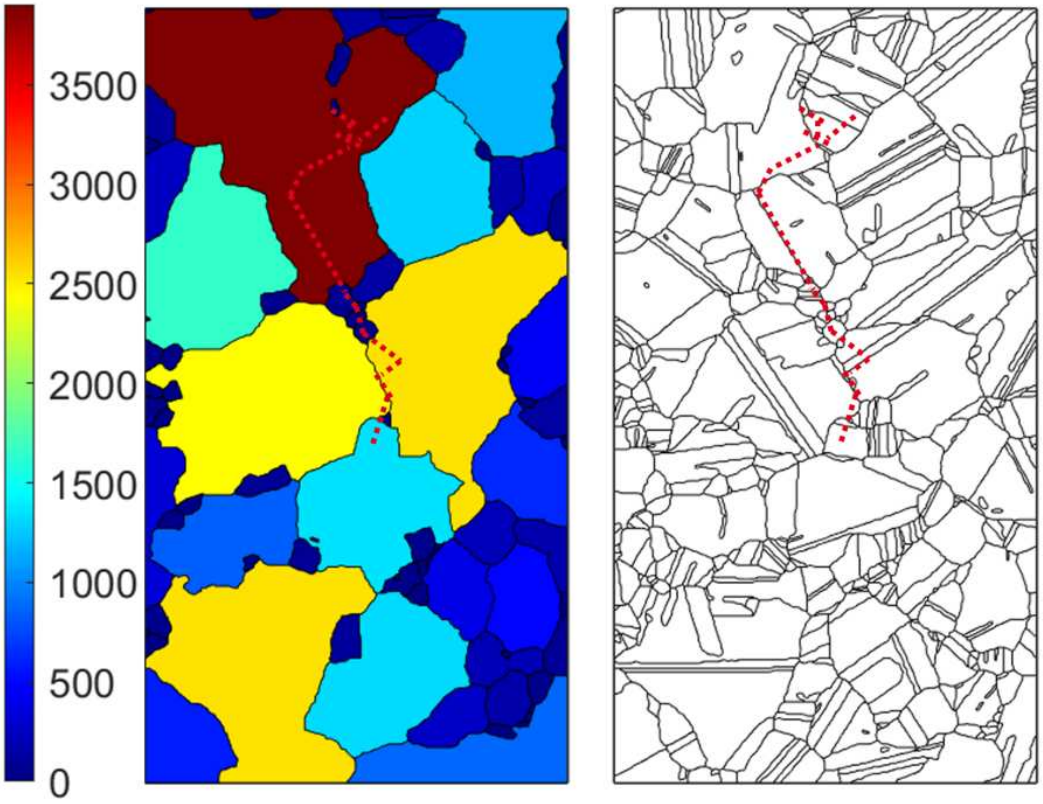

Fig. A.5 Grain cluster map (left) as a function of grain cluster area size (in μm^2) and the crack path annotated with a red dotted line as in fig. A.4. The crack overcame a few HAGBs before coming to a stop within a small grain that is part of the light blue grain cluster.

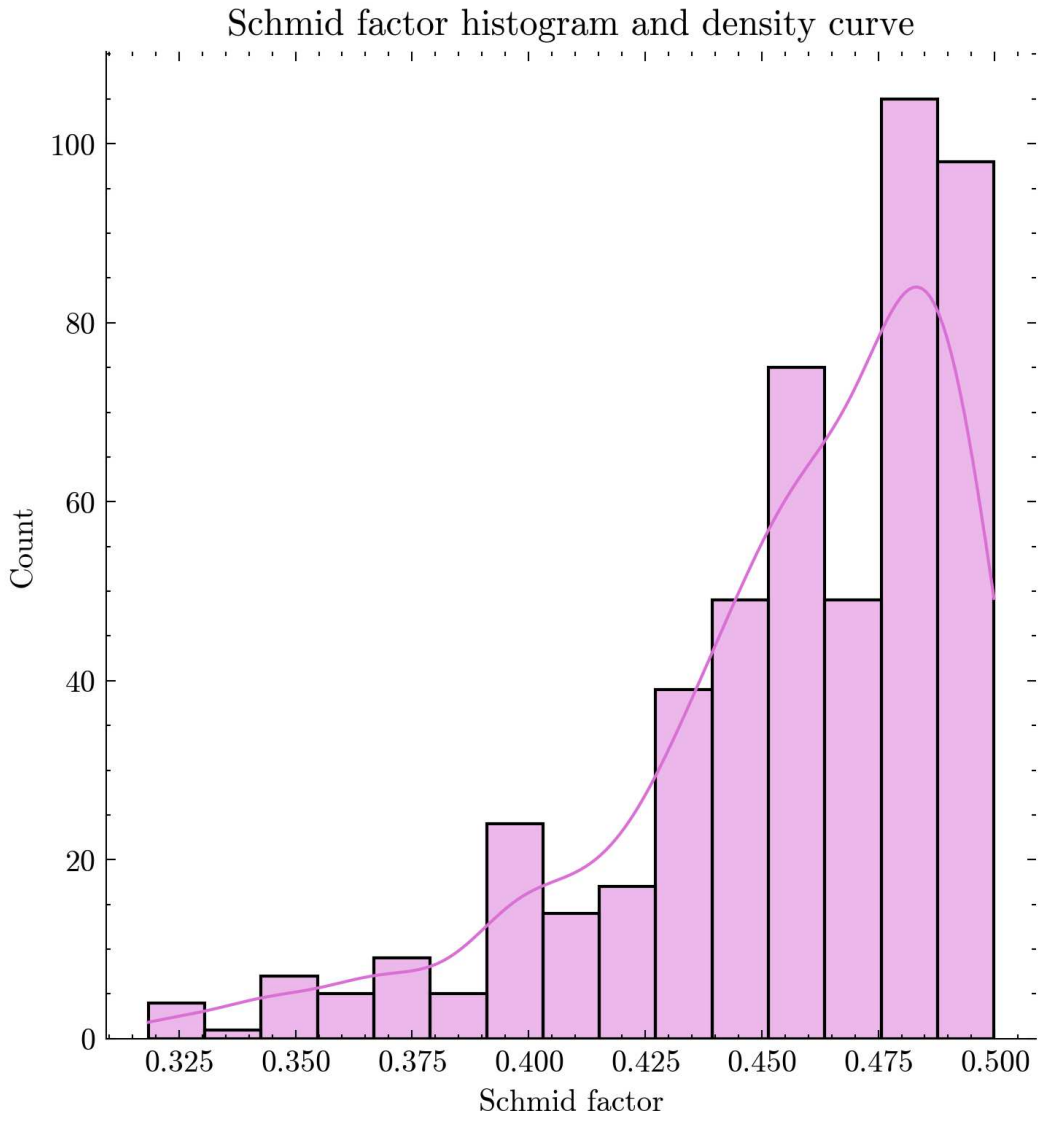

Fig. A.6 Schmid factor histogram with a superimposed density curve showing the distribution of a random selection of 500 grains from a tested sample. The average value was evaluated for 0.456.

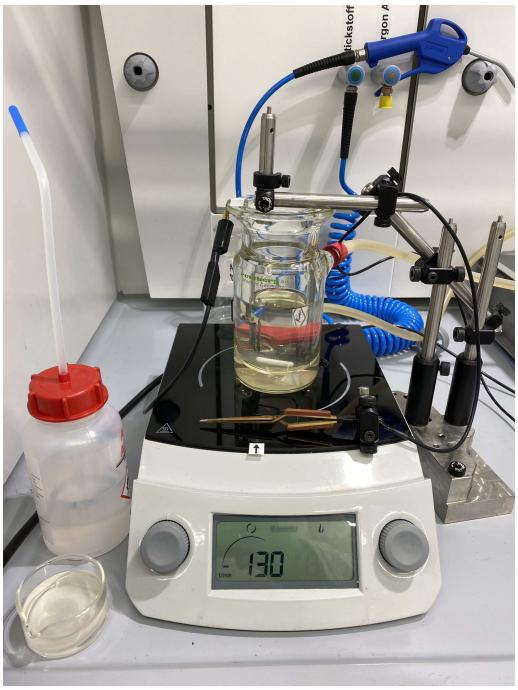

Fig. A.7 Electropolishing setup including the magnetic table set to a speed of 130 rpm, the double-walled glass cylinder, and the electrode inside with the electrolyte. The pliers in the front are then mounted above the cylinder holding the specimen.

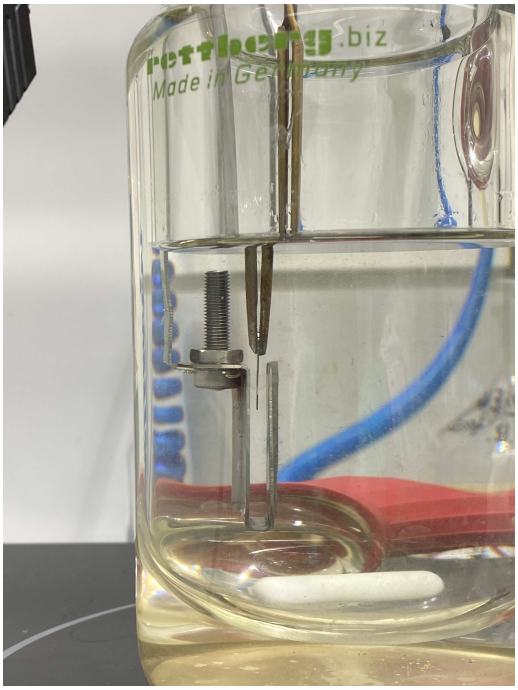

Fig. A.8 Detail of the electropolishing process where the specimen is placed between the u-shaped electrode and is ready to be polished.